Master's Thesis

A physically based FRP Sandwich Model implementing the Resin Uptake of Balsa Wood as Core Material

Tobias Otten
Matr.-Nr.: 458359

11. September 2020

Betreut von:
Prof. Dr.-Ing. Jörn Harder
(betreuender Professor)
Dr. Alexandros Antoniou
(Fraunhofer-Institut für Windenergiesysteme IWES)

FH Aachen - University of Applied Sciences
FB6 Aerospace Engineering

Eidesstattliche Erklärung

Ich versichere hiermit an Eides statt, dass ich die vorliegende Arbeit selbstständig verfasst und keine anderen als die im Literaturverzeichnis angegebenen Quellen benutzt habe.

Stellen, die wörtlich oder sinngemäß aus veröffentlichten oder noch nicht veröffentlichten Quellen entnommen sind, sind als solche kenntlich gemacht.

Die Zeichnungen oder Abbildungen in dieser Arbeit sind von mir selbst erstellt worden oder mit einem entsprechenden Quellennachweis versehen.

Diese Arbeit ist in gleicher oder ähnlicher Form noch bei keiner anderen Prüfungsbehörde eingereicht worden.

Bremerhaven, 10.09.2020
Ort, Datum

Unterschrift

Contents

List of Figures

List of Tables

List of Abbreviations

IWES	Institute for Wind Energy Systems
BWE	Bundesverband WindEnergie e.V.
VARTM	vacuum assisted resin transfer moulding
LCOE	levelized cost of energy
SS	suction side
PS	pressure side
LE	leading edge
TE	trailing edge
FRP	fiber-reinforced polymer
GFRP	glass-fiber reinforced polymer
PVC	polyvinyl chloride
PET	polyethylene terephthalate
LCM	liquid composite moulding
CLT	classical laminate theory
DIN	Deutsches Institut für Normung
ASTM	American Society for Testing and Materials
UD	unidirectional
DTU	Technical University of Denmark
SEM	scanning electron microscope
RVE	representative volume element
LD	low-density balsa
MD	medium-density balsa

HD	high-density balsa
LVDT	linear variable differential transformer
FVC	fiber volume content
FMC	fiber mass content

1 Introduction

This first chapter is meant to introduce the reader to the overall topic of industrial wind energy usage and further to specify the issue that is dealt with in this thesis. It begins with the motivation behind the thesis and a short explanation of the company where the thesis has been performed. Then, the usage of composite sandwich structures in wind turbine blades and the manufacturing process is described. Afterwards, the state of the art concerning the modelling of balsa wood with reference to related work is presented. An existing model for sandwich composites with a rigid foam core is briefly described, as it is the basis for the balsa core model, which is derived within this work. The chapter closes with stating the scope and finally the research goals of this thesis.

1.1 Motivation

Electrical energy is an essential need that has to be satisfied and the usage of renewable sources of energy is indispensable regarding the anthropogenic climate change. In order to replace fossil fuels by renewable energy sources, already existent technologies have to be enhanced to increase economical effectiveness in a relatively short amount of time. Additionally, the source of energy has to be sufficiently available.

Wind energy is one of the most available renewable energy sources in Germany, especially in the northern coastal regions. Hence, there has been a vast expansion of wind energy turbines in that regions both onshore and offshore. According to the Bundesverband WindEnergie e.V. (BWE), the total number of wind energy turbines in Germany equals to 30,925 (status: February 2020). With a total power of 61.428 GW, wind energy systems contribute 24.4 % to the total net production of electrical power in Germany. In 2019, thereby, wind energy outruns brown coal for the first time and becomes Germany's most important source of energy [1].

During the last 40 years of wind energy system development a trend can be seen concerning the size of wind energy turbines towards larger wind turbines [2]. An increase in the size of the wind turbine basically means an increase in height and in rotor blade length. In 1983 the average blade length was about 10 m. Nowadays rotor blades with up to 80 m or more have been built. One reason for this development is the fact that the generated power is proportional to the circular flow-through area of the wind turbine. Thus, a larger diameter leads to a higher power generation, assuming enough wind is available. Additional reasons are mainly driven by effectiveness, costs, maintenance and logistics. For example, in higher altitude there is more wind available, which increases the effectiveness. More effective larger wind turbines might replace a higher number of smaller wind turbines, which will then lead to less effort in maintenance. As explained later in this chapter, larger wind turbines rotate at lower speed. This is more quiet and calm to watch, so it increases the acceptance of wind turbines among residents. With regard to offshore sites, the enormous effort of transport and installation is only worth it using big sized rotor blades.

The sizing towards larger rotor blades has been done with respect to the theory of similarity, based on experience [3]. Accordingly, the upsizing process obeys the following aspects:

- maintaining of the tip speed ratio λ
- maintaining of aerodynamic profiles, blade number and material
- change of all dimensions to the same ratio, i.e. using the same scaling factor

The tip speed ratio λ is the ratio of the circumferential tip speed u and the wind speed v. Maintaining this ratio means a reduction of the angular speed of wind turbines with higher blade length. With regard to these sizing rules, the aerodynamic loads are increased proportionally to the square of the multiplier, whereas the mass is proportional to the cube of the multiplier. This square-cube law indicates, that research on proper mass estimation is highly relevant in the design and sizing process of rotor blades.

The conditions named above lead the developing and manufacturing wind energy industry to the focus on lighter, high-performance materials to further reduce the levelized cost of energy (LCOE), i.e. the cost of producing electrical energy over a wind turbine's lifetime. Due to large differences in dimensions of test material and the finished parts, blade design involves risks and uncertainties that have to be faced with validated models, which are able to predict structural parameters and material's performance. Hence, they are enhancing the risk reduction during the service life of a turbine [4, Material and component testing].

With respect to the actual topic of this thesis the enormous importance of mass estimation is stated by the fact that a proper estimation significantly depends on the amount of absorbed resin that penetrates the core of sandwich structures of a rotor blade. About 75 % of the skin area are designed as sandwich structures [3] and the density of resin is way higher than the density of balsa wood. Modelling this resin uptake in a manner close to reality will contribute to the strengthening of wind energy utilization. An additional purpose of the model is the quantitative calculation of the stiffnesses of the resin-infused core, especially the shear stiffness and the bending stiffness. It can be assumed that the resin-filled core shows up an increase in stiffness. Models with proper predictions could help to use this higher stiffness within the rotor blade design in order to optimize the stiffening structure to gain further weight reduction.

1.2 Company: Fraunhofer Institute for Wind Energy Systems (IWES)

The Fraunhofer Institute for Wind Energy Systems (IWES) is part of the Fraunhofer-Gesellschaft, which is a German research organization undertaking applied research for the purpose of economic development and contributing to the benefit of society [4, About us]. Founded in 1949, there are currently in total 74 institutes and research units in the Fraunhofer-Gesellschaft working in international collaborations with excellent research partners around the world and covering today's new innovative technologies. Those worldwide partnerships ensure direct access to regions of the greatest importance in order to make new technologies affordable and applicable. In particular the institutes of the Fraunhofer-Gesellschaft play an important role in Germany and Europe by strengthening the technological base and thus the economical acceptance of new technology. Furthermore its work includes the education and training of the future generation of scientists and engineers [5].

The Fraunhofer IWES was founded in 2009 and thus it is one of the youngest institutes of the Fraunhofer-Gesellschaft. With its entire focus on wind energy the IWES offers turbine manufacturers, suppliers, wind farm operators and power authorities a large variety of research services and target-oriented collaboration covering complete technical aspects of wind energy utilization [4, Startpage]. At the location in Bremerhaven, Germany, one main focus is the qualification of composite materials and components of rotor blades as central components of wind energy turbine systems. That competency may be subdivided into three disciplines: full-scale blade testing, rotor blade manufacturing and material and component testing. The full-scale blade tests are performed in huge test facilities that allow the testing of blades with a length of up to 100 m. Both static and cyclic testing is possible, moreover, virtual testing [4, Full scale blade testing].

As rotor blades of wind energy turbines consist of modern lightweight structures, Fraunhofer IWES has a broad expertise in manufacturing, testing and characterizing fiber-composites. It is capable of manufacturing material samples in accordance with customer specifications and offering standard tests. In addition, rotor blade components are tested. The aim is, to characterize new structural components, which are highly critical and structurally relevant, such as bonded joints, ply drops, spar caps and blade trailing edges. Fatigue tests also provide the possibility to determine the properties of adhesives for example [4, Material and component testing].

1.3 Composite Sandwich Structures in Wind Turbine Blades

From the structural side the rotor blade of a wind turbine consists of several structure parts which together form the blade's profile.

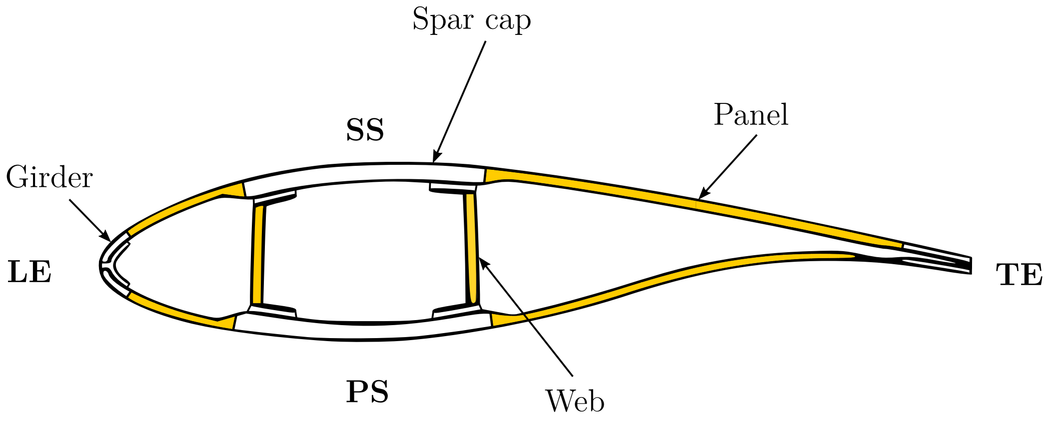

Figure 1.1: Blade profile [6, mod.]

As shown in Fig. 1.1, a cross-sectional view depicts all structural elements, the blade consists of. The aerodynamic shell can be divided into the upper suction side (SS), where lift is acting as negative pressure, i.e. a suction force and the lower pressure side (PS), where a positive pressure force is contributing to the lift. Further, the frontal nose edge is referred to as leading edge (LE), whereas the converging edge is the so-called trailing edge (TE). The main carrying structural parts are the girders both on leading edge and trailing edge and the spar caps. These parts represent the primary structures. Moreover, the secondary structures are represented by two webs and the panels, which form the closed shell [6].

Regarding the carried loads, the primary structures of the rotor blade are supposed to withstand the occurring bending moments. In operation there might occur two different bending motions, the flap-wise bending and the edge-wise bending. Flap-wise bending describes a motion that is mainly driven by the acting lift on the rotor blade, i.e. the blade is bent around its transverse axis. This acting moment is carried mainly by the spar caps. A bending around the axis, which is perpendicular to the longitudinal-transverse plane of the blade, is called edge-wise bending. Edge-wise bending moments are carried by the girders both at LE and TE [6].

When it comes to the secondary structures, the purpose is different. The webs and panels are designed to offer sufficient large stiffness against shear loads and to provide torsional stiffness. These requirements are equivalent to a high resistance against buckling. Especially thin-walled cylindrical and airfoil-shaped structures are prone to buckling. Therefore those structures and especially the secondary structures of a rotor blade are usually designed as a sandwich [3, 7].

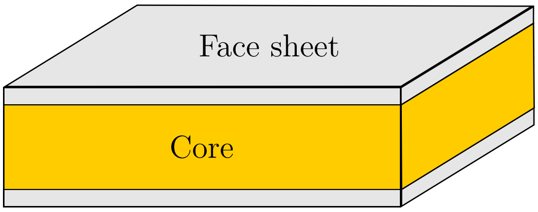

Figure 1.2: Sandwich structure

Sandwich structures as depicted in Fig. 1.2 are thin-walled lightweight structures consisting of a core material and covered by thinner face sheets. The face sheets are composite structures made of fiber-reinforced polymer (FRP). In case of the panels and webs in rotor blades it is common to use glass-fiber reinforced polymer (GFRP). In GFRP glass-fibers are embedded in a surrounding matrix made of hardened epoxy resin. The face sheets are mainly the carriers of tensile and compressive forces. The sandwich core, however, has several other functions. Its material varies primarily from different kinds of rigid polymer foams, such as polyvinyl chloride (PVC) foam or polyethylene terephthalate (PET) foam, to balsa wood. With a density of roughly

10 % of the face sheet resin's density the core material is much lighter per volume than the face sheets. Such a small density is required with regard to the larger thickness in comparison to the thin face sheets. In order to increase the bending stiffness, one main function of the core is to define a certain distance between the face sheets. That distance defines the height of the sandwich structure's cross-section and thus its area moment of inertia. The core is also meant to absorb the occurring shear loads [3, 7].

The sandwich panels have to be formed in a way to follow the curved aerodynamic shell of the rotor blade. In order to allow the core plate's adjustment in the curved geometric form, the core plate is contoured. That means that the core plate is cut in a regular defined pattern. Balsa wood core plates are usually cut into small rectangular blocks, which are held together by a glass-fiber fabric, that is glued to one surface of the balsa wood plate.

1.4 Vacuum Assisted Resin Transfer Moulding (VARTM)

The vacuum assisted resin transfer moulding (VARTM) is a manufacturing method for composite components. Both simple composite plates and sandwich plates are manufactured applying this method. But also way more complex structural parts or components like beam profiles can be built with VARTM. The VARTM is one variant of the so-called liquid composite moulding (LCM). Figure 1.3 shows the infusion process in principle.

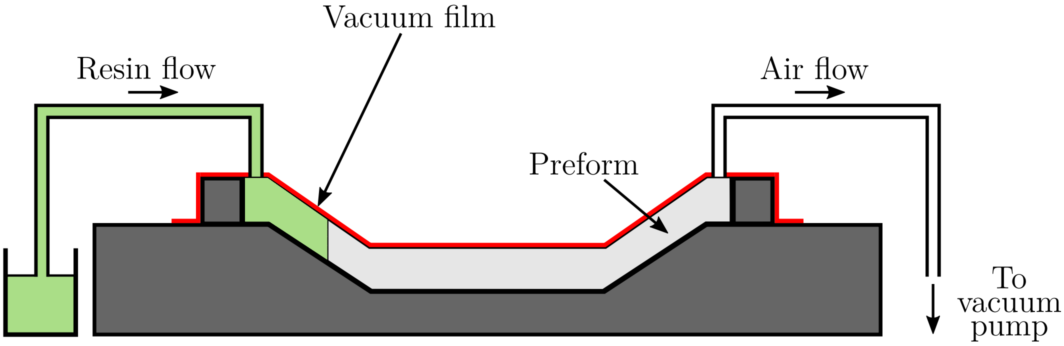

Figure 1.3: VARTM infusion process

In a first step the dry fiber layers are cut into suitable dimensions and stacked in desired order. The stacking of the layers is done on a heatable surface, e.g. a flat table or a curved mould. When manufacturing a sandwich, the core is placed between the fiber layers. This dry stacked structure is called the preform. Now the resin infusion has to be prepared. In order to ensure a smooth and even resin penetration throughout the whole component, further special layers have to be applied to the preform. The preform is then covered by a transparent vacuum film, which is fixed air-tight. With a vacuum pump the air is sucked out and the film is pressed tight onto the preform. Then the resin is mixed with a hardener, freed from gas and lead into the preform-vacuum build-up. After the preform has been completely infused by resin, the component has to be cured over time at predefined temperatures to become a solid. The component can then be demoulded and trimmed to its final measures [8].

In the wind turbine industry this process is well adapted. Especially when it comes to sandwich components, LCM is advantageous due to its possibility to manufacture the whole sandwich in a single infusion. This process goes along with the resin uptake of balsa wood as core material in sandwich components [3, 7].

1.5 State of the Art/Related Work

The panels of today's wind turbine blades are usually designed as sandwich in order to achieve a sufficient stiffness against buckling [7]. While the sandwich's face sheets are made of FRP, different core materials are available. Commonly used core materials are balsa wood or rigid foams, such as PVC or PET foam. The sandwich's core kits are manufactured with slits (contoured) to allow their adjustment in the curved geometric form. Both the horizontal and vertical slits of the contoured core and the truncated cells of the balsa wood at the core's surface are penetrated by a non-neglectable amount of resin that contributes to mass and stiffness [7].

Within the design phase of rotor blades it is essential to be able to have accurate means for the estimation of mass and stiffnesses. Those means are usually analytical or FE models. In particular the modelling of the core of sandwich structures poses a challenge since the resin uptake has to be considered realistically. Models, which neglect the resin uptake do not offer a proper estimation of mass and especially when it comes to a buckling analysis, the negligence of the resin that penetrates the core can be critical [7]. Existing models of balsa wood as pure material without resin are able to predict mechanical properties in an accurate way taking the dependency on density into account. For instance mechanical investigations have been done by Vural and Ravichandran [9] and Da Silva and Kyriakides [10]. Equations for stiffnesses and mechanical properties for wood in general are stated by Gibson and Ashby [11] on a cellular level. These equations are further used by Easterling et al. [12] to perform a relation of balsa wood microscopy (cell geometry) to mechanical strength. The microscopic structure of balsa wood is given in detail by Borrega et al. [13] using a scanning electron microscope (SEM) and evaluating the micrographs. A modelling approach of dry balsa wood (without resin uptake) has been done by Shishkina et al. [14] including different cell types.

The impact of resin uptake of a contoured rigid PVC core has been investigated by Rosemeier et al. [7]. The model considered implemented resin slits only in longitudinal direction of the core plate and was meant to gain infused-core properties in order to make them comparable to dry-core properties. The properties of the infused core have been gained by applying the so-called smearing method as it has already been done by Nickel [3] who developed an analytical model implementing the resin uptake of a quasi-isotropic rigid foam core for GFRP sandwich composites.

Nickel's model shows accurate results for core material having cells of spherical shape and of one type. Balsa wood in contrast consists of more than only one cell type. Its cells differ in size, shape and orientation and are strongly dependent on material density [13]. None of the balsa wood cell types physically has a spherical shape. Due to major dissimilarities in the microscopic structure between balsa wood and rigid foam (e.g. PVC foam), the amount of resin that penetrates the truncated cells and thus the resulting mass and stiffness is different. Additionally, balsa wood is an orthotropic material and thus its mechanical properties significantly depend on direction [12]. These facts lead to the need of a physically based FRP sandwich model implementing the resin uptake of balsa wood as core material. The model from Nickel shall serve as basis for the new model of the infused balsa wood core.

1.6 Scope and Research Goals

The master's thesis deals with the resin uptake of balsa wood as core material for sandwich plates with FRP facings. Because of the liquid composite moulding manufacturing, the uptake effect may have a significant influence on mass as well as on shear and bending stiffness and thus on buckling resistance of a component. The large panel areas of the aerodynamic sandwich skins of the wind turbine's rotor blade are expected to be affected the most.

The aim of the thesis is the adaptation of an existing analytical model for the rigid foam core (e.g. PVC) that will accordingly be modified and implemented in order to simulate properly the resin uptake of a balsa wood core.

Both truncated balsa wood cells and the slits of the contoured core plate are filled with a significant amount of resin before hardening. A physically based model is developed, build on the Balsa wood micro-structure, proper for mass uptake estimation and prediction of the mechanical properties of sandwich configurations that result after the manufacturing and the curing process. The physical and mechanical properties of the sandwich panel's constitutive materials i.e. the balsa and the polymer resin will be smeared through analytical formulations. In addition, a pure geometrical approach is implemented to estimate the mass uptake. In order to calculate the stiffnesses of sandwich and infused core, the classical laminate theory (CLT) is used. For the essence of the model validation, sandwich specimens will be manufactured. These will be tested mechanically via a four point bending configuration according to international standards. The work of this thesis shall focus on plane plates without curvature. The derived analytical model is set up on a Microsoft Excel spread sheet including various options for the setting of necessary parameters and all calculations.

The scope of this thesis comprises in detail:

- literature research on the micromechanical structure of balsa wood and on "smearing" of mechanical properties of a multi-phase medium
- description of the adapted analytical model regarding the calculation of mass/-density and stiffnesses of resin and core material
- tests in order to investigate material behaviour of balsa wood
- manufacturing of resin-infused core plates to validate mass estimation
- detailed four point bending tests with own manufactured sandwich specimens in accordance with engineering standards
- comparison of the analytic model and the experimental results

2 Theoretical Work

The essence of this chapter is the presentation and description of the newly derived analytical model of a plane sandwich plate with a resin-infused balsa wood core. The following sections are meant for deriving the geometries and mathematical approaches, that lie behind the calculations implemented in the model. When describing the resin-infused core model it is distinguished between mass calculation including its different approaches and stiffness calculation. However, the stiffness calculation of the overall sandwich component is done using the equations stated in the CLT. Therefore the CLT is explained in detail in an own section. Finally, the theory behind the four point bending test and a comment on the choice of the underlying engineer standard is presented.

2.1 Microscopic Structure of Balsa Wood

Wood in general is made of different types of cells with large variations in size and shape depending on its natural growth and the biological function of each cell type. Balsa wood (Ochroma pyramidale) is classified as hardwood and grows in tropical regions ranging from southern Mexico to Bolivia. The fact that balsa is a naturally growing tree, makes it impossible to define constant material properties without a relation to the density. The density varies within a broad range from about 40 $\frac{\mathrm{kg}}{\mathrm{m}^3}$ up to 380 $\frac{\mathrm{kg}}{\mathrm{m}^3}$. Physically the difference in density goes along with a difference in the size of the different cell types [13].

To gain a sound knowledge on how the cells are oriented within a fabricated balsa wood plate, it is necessary to know, how the fabrication is done. When fabricating balsa wood plates as core material, the lumbered tree trunks are cut into long cuboids. The main sap channels, later in this section referred to as vessel cells, are orientated in longitudinal direction, since they lie vertically inside the trunk of the non-lumbered tree. After sorting according to density ranges, the sorted wooden cuboids are glued together. A plate of balsa wood is then gained from cutting slices [15, slides 23-30].

That means that the final delivered core plate is actually a composite made of several different trees roughly sharing the same density range. For this work, the balsa wood plates have been purchased from the company Gaugler & Lutz oHG. Here, for the reason of categorization, a specific denomination is attributed to each plate labeled with the apparent nominal density and the minimum sheet density. That will be important later, when the features of the model are introduced.

In order to see, how balsa wood is structured in detail, it is essential to have a look at microscopic pictures. Within the scope of this thesis, balsa wood pieces have been investigated at IWES using an optical microscope. However, the spectated samples did not show adequate details on the balsa's surface. This can be explained by the fact that the surface of the balsa wood was not prepared in particular, so it was assumed that the surface was way too rough. Nevertheless, detailed surface structures could be seen to a very small extend. In addition to these attempts of picturing the cells of balsa wood, some samples of balsa wood have been sent to both the Fraunhofer IWES in Hannover and the Technical University of Denmark (DTU). Both institutes have the possibility of taking x-ray scans to generate microscopic pictures.

With regards to a faster progress in specifying the model, the decision was made to focus on published literature to define the balsa wood's micro structure. Later comparison to the received x-ray scans showed a good accordance to the measured values from Borrega et al. [13]. So for modelling the balsa wood's cell structure, the literature from Borrega et al. is used. The main reason for choosing that literature is that it delivers detailed and high-resolution pictures of balsa wood taken by a SEM. Additionally, the cell geometries have been measured accurately multiple times and throughout a wide range of densities. Besides, the literature from Easterling et al. [12] also shows simplified cell geometries of medium dense balsa samples, giving values for lengths, widths and cell wall thicknesses. In the paper from Shishkina et al. similar cell geometries are illustrated.

When having a look at the trunk's cross-section, a three-dimensional coordinate system can be defined, marking the radial direction, the tangential direction and the vertical axial direction. For the balsa plate's coordinate system though, this definition is not applicable, because the plate is made up of many different cuboids, which are turned arbitrarily about their axial direction. Hence, the xyz-coordinate system is further used to describe directions and planes of the balsa plate (see Fig. 2.1).

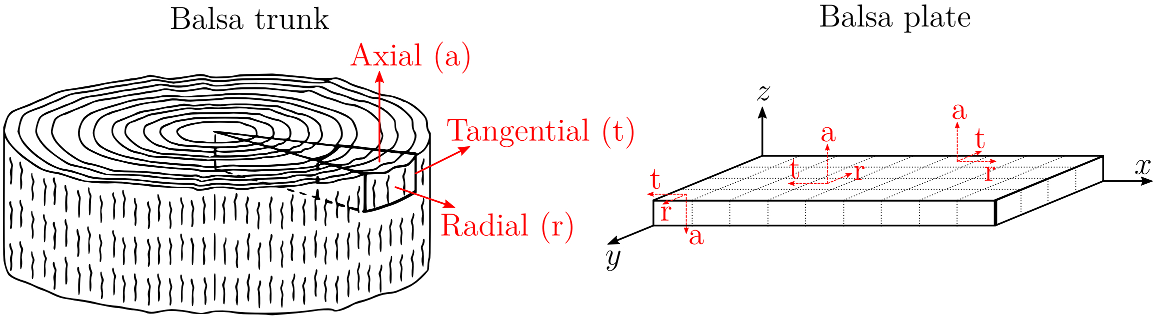

Figure 2.1: Coordinate systems of balsa trunk and balsa plate [10, mod.]

Basically, balsa wood consists of three different cell types: vessels, rays and fibers. Those cells can be distinguished easily, as shown on the SEM picture (Fig. 2.2).

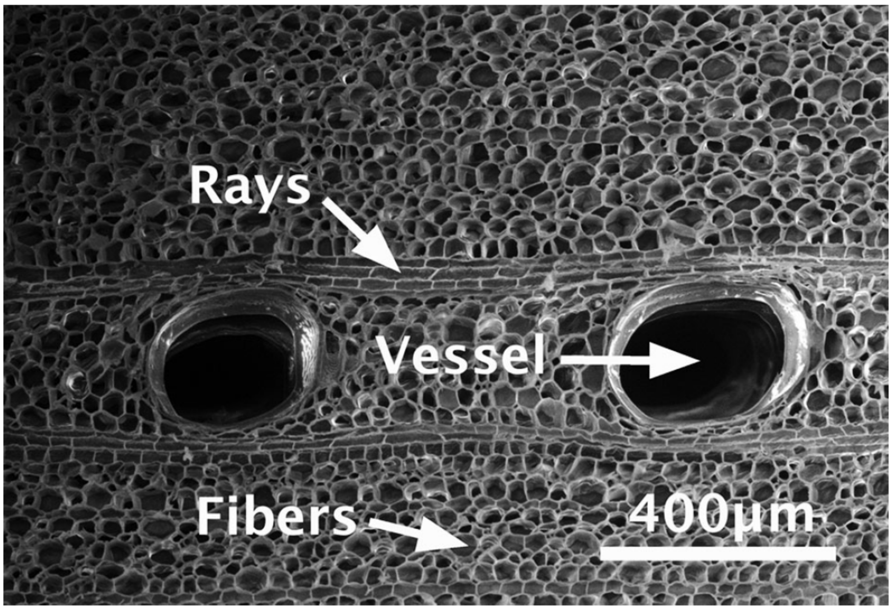

Figure 2.2: SEM micrograph of balsa wood [13]

The perspective in Fig. 2.2 is in that way, that the view is pointing at the top (or bottom) surface side of a balsa wood plate. The vessels' direction is equal to the direction of plate thickness, further called the z-direction.

The vessel cells (Fig. 2.3) are the largest ones and have an elliptical shape, elongated in radial trunk direction and defined by the diameters D and d, where D is the larger one and d is perpendicular to D. As the only balsa cell type, the vessel cell can be seen as one continuous cell that reaches from end to end in z-direction. In fact, it is composed of short elements, which have the defined length L. Some vessels are grouped together and their adjacent cell walls are flattened. The cell wall has been measured between the cell lumens, so the measured cell wall t is actually the double cell wall between two neighbouring cells. Vessels however have a thicker double cell wall T when adjacent to other vessel cells. In some literature the vessels are also referred to as sap channels due to their purpose of directing the cell sap through the trunk.

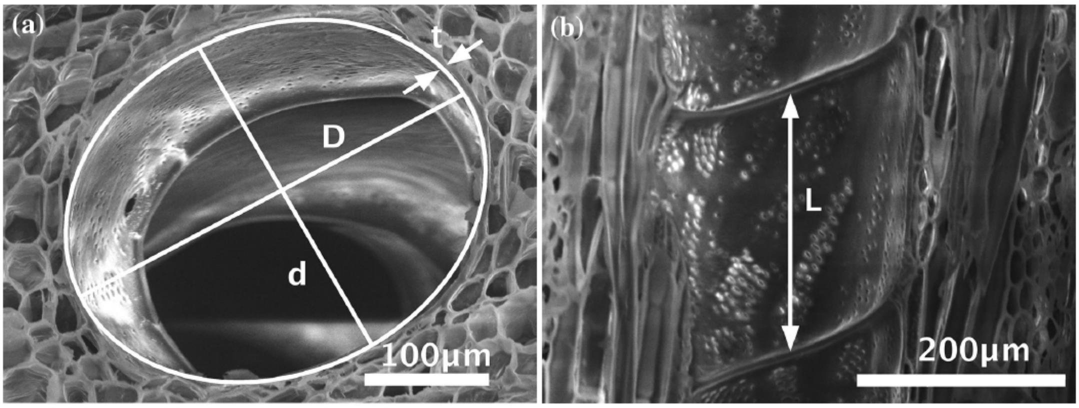

Figure 2.3: SEM micrograph of a vessel cell: (a) view on xy-plane (b) view on lateral plane [13]

The second type of cells are the ray cells as seen in Fig. 2.4. This cell type is arranged in thin lines, which grow in radial direction of the trunk. When viewed from above they have a rectangle geometry with the long edge a and the short edge b. A cross-sectional view on the lateral xz-plane or respectively the yz-plane however, reveals a more oval shape. The cell height is denoted as L.

Figure 2.5 shows the third cell type of balsa wood, the so-called fibers. With roughly 65-75 % these cells share the highest volume fraction of all balsa cell types. Fiber cells are long cells, elongated in z-direction and pointed at the ends. Looking at the xy-plane those cells show an irregular hexagonal shape. In order to give them a regular shape, which is suitable for modelling, the fiber cells are assumed to be regular hexagons with the cell edge having the length h. The total vertical length of the fibers is denoted as L. The wast majority of the fiber cells are practically assumed to be straight vertical. However, there are some fibers, which are misaligned by the angle θ. In Fig. 2.5 (b) it can be seen that some sporadic fibers are occasionally divided by

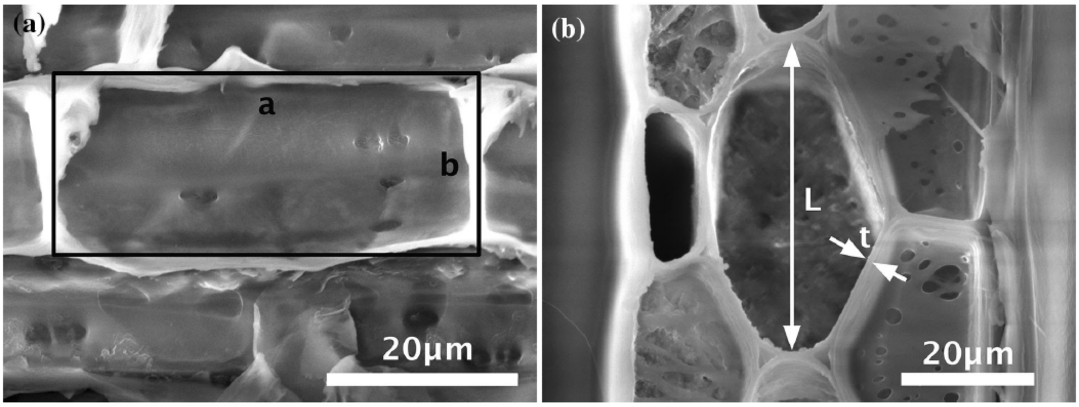

Figure 2.4: Ray cells: (a) view on xy-plane (b) view on lateral plane [13]

transverse cell walls. These walls are in particular described by Easterling et al. [12], although they are not mentioned at all by Borrega et al. [13]. The white arrows in Fig. 2.5 (b) indicate a fourth cell type, the so-called parenchyma cells. Beside the other three basic cell types, the parenchyma cells are difficult to identify when looking at the xy-plane. Therefore, this cell type is neglected for modelling.

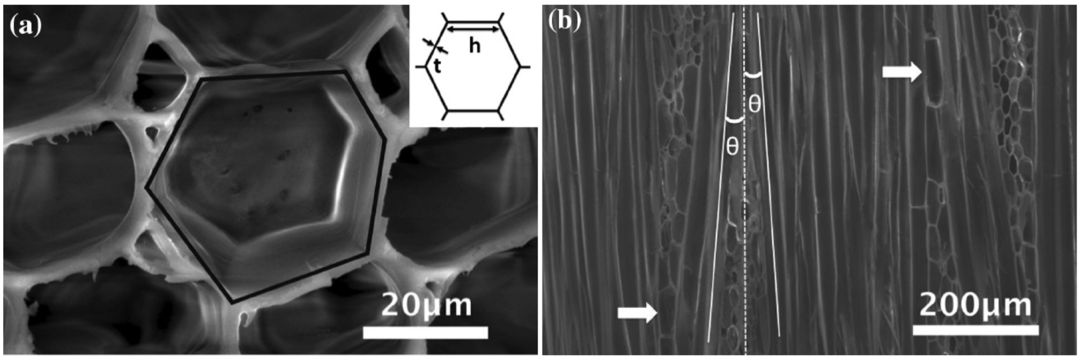

Figure 2.5: SEM micrograph and model of fiber cells: (a) view on xy-plane (b) view on lateral plane [13]

The paper from Borrega et al. summarizes the measurements of the balsa cell geometries in a table (Table 2.1). In doing so, the measurements are sorted by density, subdividing the broad density range into three density classes. Balsa wood with a density of less than 100 $\frac{\text{kg}}{\text{m}^3}$ is denoted as low-density balsa (LD) and medium-density balsa (MD) shows a density between 100 $\frac{\text{kg}}{\text{m}^3}$ and 200 $\frac{\text{kg}}{\text{m}^3}$, whereas samples with a density higher than 200 $\frac{\text{kg}}{\text{m}^3}$ are categorized as high-density balsa (HD). The table below shows mean values for the air-dry density (moisture content of balsa wood between 5 % and 7 %) of all three density classes.

Table 2.1: Dimensions, volume fraction and solid fraction of main cell types in balsa wood of different densities [13]

	LD balsa	**MD balsa**	**HD balsa**
Air-dry density [$\frac{kg}{m^3}$]	64	163	274
Vessels			
D [µm]	220.4 ± 31.0 (14)	320.8 ± 31.1 (23)	258.8 ± 38.6 (39)
d [µm]	156.6 ± 21.5 (14)	251.0 ± 18.5 (23)	206.6 ± 24.0 (39)
L [µm]	n.d.	382.1 ± 121.1 (19)	n.d.
t [µm]	n.d.	4.0 ± 1.1 (99)	n.d.
T [µm]	n.d.	9.5 ± 1.5 (70)	n.d.
Volume fraction [%]	2.8 ± 0.5 (4)	6.6 ± 1.1 (4)	8.8 ± 2.1 (8)
Solid fraction [%]	6.8	4.5	5.5
Rays			
a [µm]	49.6 ± 8.4 (23)	35.8 ± 6.1 (34)	32.5 ± 3.5 (34)
b [µm]	19.4 ± 3.3 (23)	18.2 ± 3.1 (34)	15.8 ± 1.7 (34)
L [µm]	n.d.	30.7 ± 6.0 (60)	n.d.
t [µm]	n.d.	0.9 ± 0.3 (97)	n.d.
Volume fraction [%]	20.9 ± 2.1 (4)	19.9 ± 0.8 (3)	24.8 ± 1.9 (7)
Solid fraction [%]	6.5	7.4	8.3
Fibers			
h [µm]	21.8 ± 4.5 (57)	18.0 ± 4.8 (105)	9.8 ± 3.0 (270)
t [µm]	0.8 ± 0.2 (50)	1.8 ± 0.5 (125)	2.2 ± 0.8 (250)
L [µm]	n.d.	755.3 ± 122.2 (38)	n.d.
θ [°]	n.d.	6.1 ± 2.0 (30)	n.d.
Volume fraction [%]	76.3	73.5	66.4
Solid fraction [%]	4.3	10.8	21.5

All the given values in Table 2.1 are mean values ± standard deviation. The numbers in parentheses indicate the number of measurements of the particular measures. The values marked with n.d. have not been determined.

Having a closer look at the measured values, there are some interesting data to be highlighted. The vessel diameters D and d do not increase linearly with the wood density. Instead the diameters are the highest in MD balsa and further decrease with increasing density. Own measurements using the x-ray scans of MD balsa deliver values of $D = 293.6\,\mu m$ and $d = 222.2\,\mu m$ and the measured values are in agreement with values given in the papers of Vural and Ravichandran [9] and Da Silva and Kyriakides

[10]. The volume fractions of vessels and rays have been determined by measuring the area fraction, which equals the volume fraction assuming a constant depth in direction of view. The volume fraction is meant in relation to the total wood volume. The fibers' volume fraction is simply calculated to complete 100 %. The solid fractions have been gained from mean lumen dimensions and cell wall thicknesses and is here meant in relation to each cell type. With increasing density, the fiber cells decrease in their edge length h while their cell wall thickness increases. That is intuitive, because the cells themselves densify. This behaviour does not apply to the vessels. The showed increase of the vessels' volume fraction with increasing density is counterintuitive because of the fact that vessels are relatively large empty voids. Increased fluid transportation requirements could be an explanation.

2.2 Modelling of Balsa Wood Cell Geometries

The analytical model shall be physically based. That means that the geometry of each cell type has to be defined physically accurate according to their microscopic structure. Hence, for the model each cell type (vessel, fiber, ray) is represented by a certain shape that is ascribed to it. By assigning geometry parameters to every cell type, it is possible to illustrate the specific cell in three dimensions. The defined geometry includes the cell wall and its thickness as well as the lumen of the cell.

The model is only able to use one geometry setting per cell type. Due to large varieties in cell growth and thus in its size, cell wall thickness and shape, the decision has been made to set the parameters as average values in order to represent an average cell of the specific type. For the model then all cells of the specific type do have this average size. The cells' shape however is always regular, neglecting irregular cell shapes as they physically appear to a large extend. The cell model therefore always can only be an approximation of the real cell.

When mentioning the dependence on growth of each cell, the density of balsa wood is significant. Since a higher density goes along with a change of the parameters that describe the cell geometry, implementing this dependency is necessary. When choosing an arbitrary average density (within the vast density range of balsa wood) for the balsa wood plate, the model is then able to change the affected geometry parameters of each cell type accordingly. These dependencies, which the model uses, are values gained from literature, in the strict sense from Table 2.1 by Borrega et al. [13].

Parameters, which have been measured on balsa wood samples covering all three defined density classes, are interpolated linearly between the given average densities. When having a look at some parameters like the fiber edge length h for example, it is clearly apparent that the gradient of the interpolated density differs quite much when interpolating between LD balsa and MD balsa compared to densities between MD balsa and HD balsa. Additionally, the vessel parameters D and d both show a maximum value at an average air-dry density of $163\,\frac{\mathrm{kg}}{\mathrm{m}^3}$. Those parameters, which have not been determined for LD balsa and HD balsa (marked with n.d.), are equal to the given average value for MD balsa. All given cell wall thicknesses t are double cell wall thicknesses between two cell lumens. When defining the geometry of a cell, it is appropriate to use one single wall thickness. Therefore, the model offers the option to consider either the single wall thickness $\frac{t}{2}$ or the double wall thickness t. Here, the default option is "single wall". This option is considered to be physically accurate when describing the geometry of adjacent cells correctly.

At first the geometry of the vessel cell model shall be described. This cell has the simple geometry of an elliptical cylinder as illustrated in Fig. 2.6.

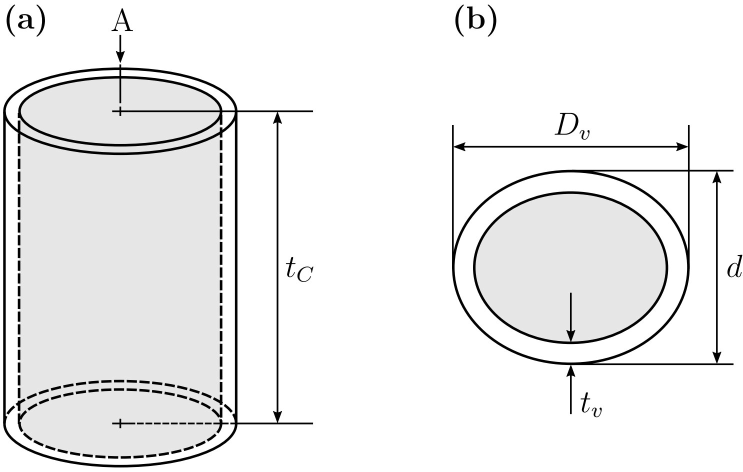

Figure 2.6: Vessel cell model: (a) 3D view (b) cross-sectional view A

The size of the regular elliptical area is defined by its major axis D_v and its minor axis d_v. Those measured lengths are assumed to cover the total lengths of the vessel cell including the cell wall t_v. As previously mentioned, SEM micrographs also show adjacent vessel cells separated by thicker cell walls T. However, this structural condition is not modelled. The vessel reaches all the way through the entire thickness t_C of the balsa wood core plate.

The elliptical model is physically accurate and primarily usable for the calculation of the empty cell volume that is supposed to be filled with resin during the resin infusion process. Hence, its exact geometry is primarily used when applying the geometrical approach of resin uptake (see Subsect. 2.3.1). The elliptical shape will be simplified into squared resin pillars when deriving the stiffnesses in Subsect. 2.4.2.

The modelled cell geometry of the ray cells is slightly more complex. The SEM micrographs identify different shapes from different perspectives. Therefore a three dimensional geometry has to be set up according to the shown pictures. Figure 2.7 shows the resulting ray cell geometry.

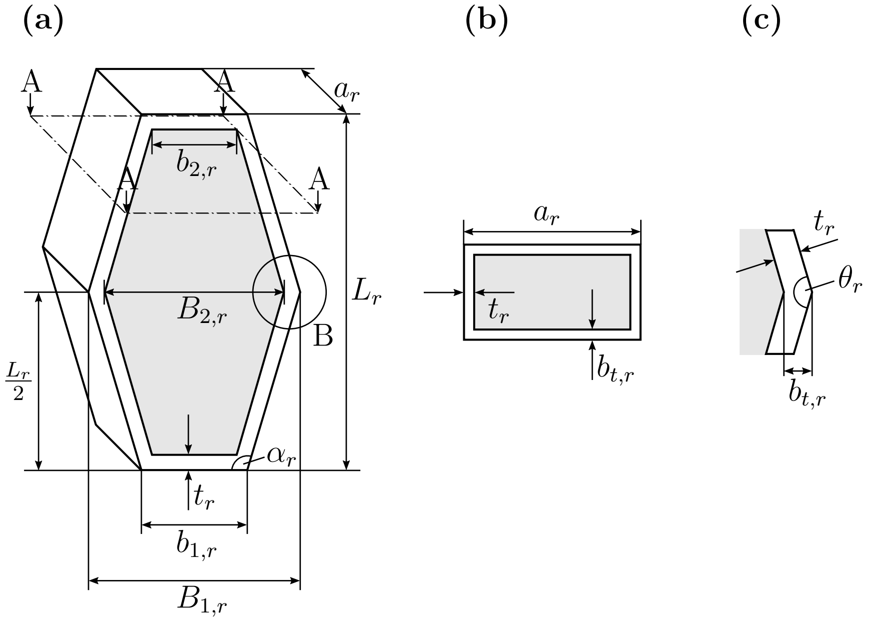

Figure 2.7: Ray cell model: (a) 3D view (b) cross-sectional view A (c) detail view B

The cell's cross-section from the lateral point of view is characterized by two trapezoids, which result by mirroring one trapezoid at its longer parallel edge. The decision to model the oval shaped cross-section in terms of trapezoids was made to allow the simple geometrical calculation of the cross-sectional area, when applying arbitrary cell cuts in order to consider the penetration depth of resin. The cell is elongated by the length a_r. The total cell height is denoted as L_r. The cell width including the cell wall thickness t_r is defined by the largest width $B_{1,r}$ at cell height $\frac{L_r}{2}$ and the smallest width $b_{1,r}$. In order to determine the inner cell widths $B_{2,r}$ and $b_{2,r}$ the cell wall width $b_{t,r}$ is gained with the help of the angle θ_r where the two trapezoids come together. In addition, there is the angle $\alpha_r = 180° - \frac{\theta_r}{2}$ needed. The mentioned geometrical parameters are calculated as follows:

$$\frac{\theta_r}{2} = \arctan\left(\frac{\frac{L_r}{2}}{\frac{B_{1,r}-b_{1,r}}{2}}\right) \tag{2.1}$$

$$b_{t,r} = \frac{t_r}{\sin\frac{\theta_r}{2}} \tag{2.2}$$

$$B_{2,r} = B_{1,r} - 2\,b_{t,r} \tag{2.3}$$

$$b_{2,r} = b_{1,r} - 2\,\frac{t_r}{\tan\frac{\alpha_r}{2}} \tag{2.4}$$

Now, the model for the last remaining balsa cell type, the fiber cell, is presented. The fiber cell is modelled as a straight pillar with a regular hexagonal cross-section and the ends pointed with the shape of a pyramid with hexagonal basis.

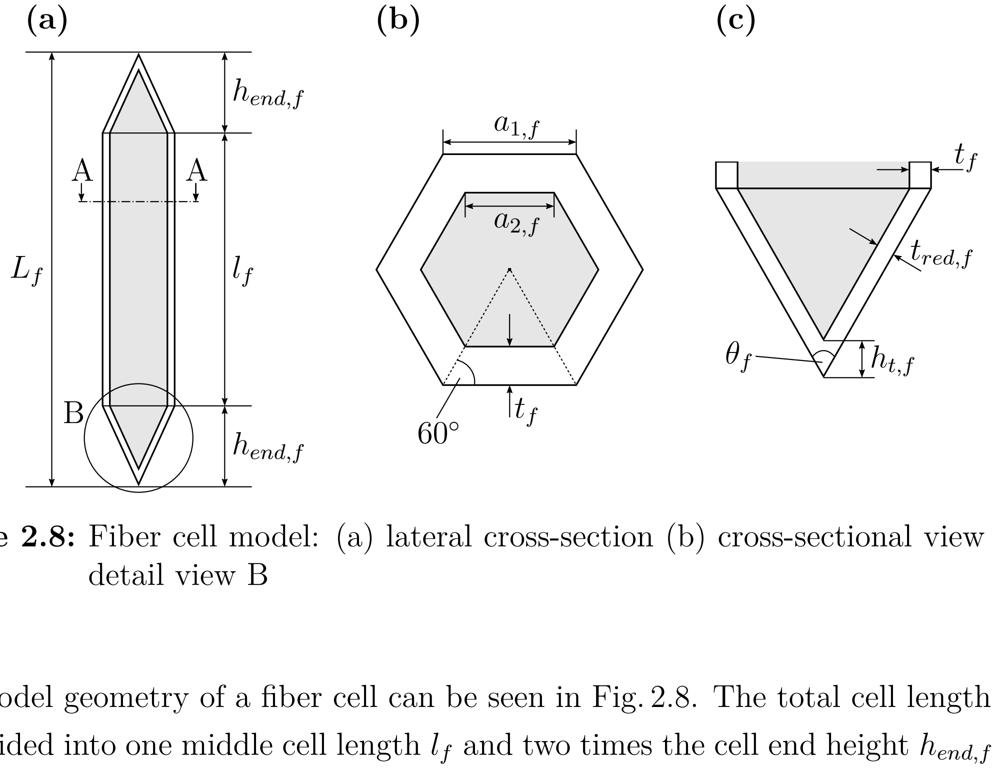

Figure 2.8: Fiber cell model: (a) lateral cross-section (b) cross-sectional view A (c) detail view B

The model geometry of a fiber cell can be seen in Fig. 2.8. The total cell length L_f is subdivided into one middle cell length l_f and two times the cell end height $h_{end,f}$. The cell wall thickness t_f is the thickness as measured in the plate's xy-plane. Therefore, another vertical cell wall length is needed to describe the vertical cell wall thickness at the end points of the pyramidal ends. This quantity is denoted as $h_{t,f}$ and it depends on the angle θ_f and further on a reduced cell wall thickness $t_{red,f}$. In reality this reduced wall thickness is assumed to be equal to the actual wall thickness t_f. However, the cell geometry had to be slightly modified to allow the volume calculation of the straight middle part separately from the converging cell ends. The hexagonal cross-section is well defined by the outer edge length $a_{1,f}$. But for the calculation of the empty volume inside the fiber cell it is necessary to define the inner edge length $a_{2,f}$ in addition. All named quantities are determined by the following geometrical relations:

$$l_f = L_f - 2\,h_{end,f} \tag{2.5}$$

$$a_{2,f} = a_{1,f} - 2\,\frac{t_f}{\tan 60^\circ} \tag{2.6}$$

$$\frac{\theta_f}{2} = \arctan\left(\frac{\frac{\sqrt{3}}{2}\,a_{1,f}}{h_{end,f}}\right) \tag{2.7}$$

$$t_{red,f} = \sin\left(\arctan\left(\frac{h_{end,f}}{\frac{\sqrt{3}}{2}\,a_{1,f}}\right)\right)\,t_f \tag{2.8}$$

$$h_{t,f} = \frac{t_{red,f}}{\sin\frac{\theta_f}{2}} \tag{2.9}$$

In the previous section it was stated that some fiber cells are occasionally subdivided by horizontal cell walls at arbitrary positions along their length. The model does not include these walls since they seem to be sporadic. Additionally, assuming the geometry to be the average would mean that the intermediate wall occurs exactly in the middle of the fiber cell. Approaches on the penetration depth also act on the assumption of either half-filled cells or arbitrarily truncated cells. Both approaches therefore averagely consider the horizontal cell walls.

2.3 Resin Uptake Modelling Approaches

The resin uptake of the balsa wood core is the essential feature to be implemented in the sandwich model. Hence, it is important to find physically accurate ways of determining the amount of resin in the balsa wood core. There are different approaches considerable and this section shall present those which have been investigated within this thesis. The first approach is purely geometrical basing on the modelled cell geometries. The determination of the average penetration depth actually is not an overall resin uptake approach on its own. It is rather a quantity that is needed for applying the smearing method. But there are different ways of calculating it. The smearing method itself is an appropriate way to deal with the properties of a multi-phase medium. It is an essential method for the resin-filled core model.

2.3.1 Geometrical Approach

With the definition of the cell geometries it seems likely to make use of those geometries in order to determine the total amount of resin inside the former empty cell volumes and the slits between the balsa blocks. The main idea is to calculate the total resin mass by adding together the resin-filled volumes (slits and cell volumes) of every balsa block. It is assumed that the vessel cells are completely filled with resin. Fibers and rays however are assumed to be filled averagely up to the half of their empty cell volumes both in z-direction and laterally. Figure 2.9 illustrates the resin-filled cell types for the geometrical approach.

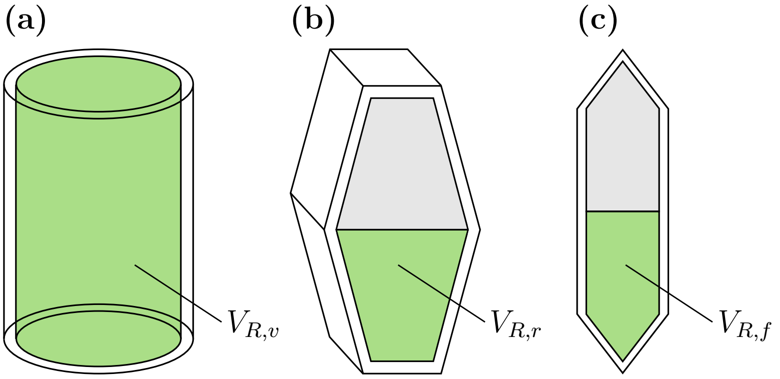

Figure 2.9: Resin-filled cell types for the geometrical approach: (a) vessel cell (b) ray cell (c) fiber cell

In a first step the resin volume of each cell type is determined with regard to the defined cell geometry. This is done by setting up the equations for the half inner empty cell volumes:

$$V_{R,v} = t_{Plate}\,\pi\,\left(\frac{D_v}{2} - t_v\right)\left(\frac{d_v}{2} - t_v\right) \tag{2.10}$$

$$V_{R,r} = (a_r - 2\,t_r)\,\frac{1}{2}\,(b_{2,r} + B_{2,r})\,\left(\frac{L_r}{2} - t_r\right) \tag{2.11}$$

$$V_{R,f} = \frac{1}{2}\,a_{2,f}^2\,\sqrt{3}\,(h_{end,f} - h_{t,f}) + \frac{3}{2}\,a_{2,f}^2\,\sqrt{3}\,\frac{l_f}{2} \tag{2.12}$$

Here, it is important to mention that all cells shall maintain their complete cross-sectional area when both vertically and laterally truncated. Furthermore, the half resin-filled cell volume stays the same independent of vertical or lateral view because the entire half cell is considered anyway. That is why only one equation for each cell type is required here.

The cross-sectional area of each cell type A_{Cell} is now determined. The aim is to gain the average number of each cell type along the surfaces of one balsa block. Together with the cells' area fractions $f_{A,Cell}$ gained from Table 2.1 (area fraction equals volume fraction) and the respective balsa block surface areas A_{Block}, the average number $N_{Cell/Block}$ of cells, which are covering all four surfaces of one balsa block can be obtained by applying the following scheme:

$$N_{Cell/Block} = \frac{f_{A,Cell}\,A_{Block}}{A_{Cell}} \tag{2.13}$$

By then multiplying the cell number per block by the cells' resin volumes as they are shown in Eqs. (2.10 to 2.12) and finally multiplying again by the total number of blocks which form the core plate N_{Block}, the total resin volume inside the cells is calculated.

$$V_{R,Cell,tot} = N_{Block}\,(N_{Vessel/Block}\,V_{R,v} + N_{r/Block}\,V_{R,r} + N_{Fiber/Block}\,V_{R,f}) \tag{2.14}$$

The remaining slit resin volume $V_{R,Slit,tot}$ is determined in a similar manner per balsa block. This requires the volume calculation of a resin frame around one balsa block measuring the half slit width $\frac{s_x}{2}$ and respectively $\frac{s_y}{2}$ on each of the four balsa block sides. This resin frame volume is multiplied by the total block number N_{Block}.

$$V_{R,Slit,tot} = V_{R,Frame/Block}\, N_{Block} \tag{2.15}$$

By means of the universal density-volume relation, the total resin mass of the pure geometrical approach $m_{R,geom}$ can be determined.

$$m_{R,geom} = (V_{R,Cell,tot} + V_{R,Slit,tot})\, \rho_R \tag{2.16}$$

For the resulting plate mass $m_{Plate,res,geom}$, the resin mass is added to the dry balsa core mass.

$$m_{Plate,res,geom} = m_{R,geom} + \rho_C\, V_{Plate,res} \tag{2.17}$$

2.3.2 Approaches on Penetration Depth

When describing the resin uptake one important quantity is the penetration depth of the resin, here denoted as t_{PD}. The penetration depth is a measure of how deep the resin reaches into the inside of the balsa wood core. This obviously depends on the cells that form the surface of the core. Due to the different shapes of the balsa cells it is necessary to indicate one penetration depth for the z-direction and one for the lateral direction. Further it is assumed that no resin is able to cross the cell wall.

As the analytical model bases on the work from Nickel [3], the determination of the penetration depth has been done according to Nickel's approach in a first step to see if this approach is applicable for the balsa wood core. The rigid foam core cells in Nickel's model are defined as ideal spheres with a cell wall having constant thickness. Across the surface of the foam core, these spherical cells are distributed quasi-homogeneously. Thus, the surface cells are truncated at different cut heights h_c. It is assumed that the resin can only fill the truncated surface cells and that the cell wall is not permeable to resin. So the inner cell volume is equal to the volume $V_{R,c}$, which is dependent on h_c. Further, the cutting area A_c is needed. It represents the entire cross-sectional cell area at the cut height h_c inclusive of the cell wall with its thickness t_{sph}. The average total radius of the spherical cell is R_c.

Now the idea of how to gain the penetration depth is to divide the cell's resin volume $V_{R,c}$ by the area A_c. With regard to the units this makes sense. The actual physical meaning of this approach however may not be clear at first glance, but it can be visualized using the example of the spherical cell as shown in Fig. 2.10:

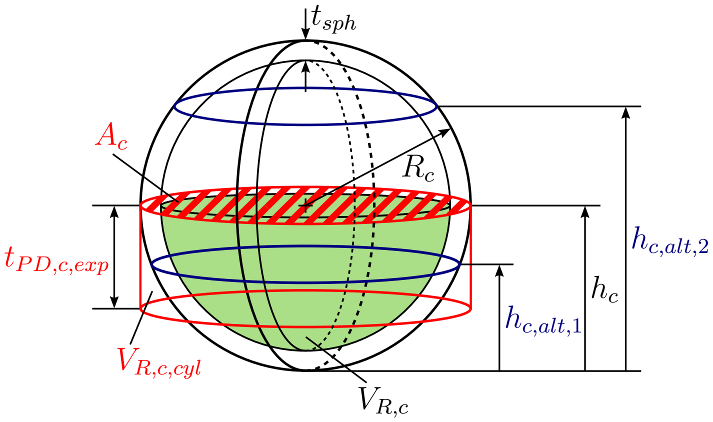

Figure 2.10: Nickel's approach on penetration depth

Following the approach's way to determine $t_{PD,exp}$, the following exponential equation is applied:

$$t_{PD,c,exp} = \frac{V_{R,c}}{A_c} = f_1(h_c) \tag{2.18}$$

After simply rearranging Eq. (2.18), the resin-filled volume of the truncated cell can be seen as the volume of a cylinder $V_{R,c,cyl}$ having the base area A_c and the height $t_{PD,c,exp}$.

$$V_{R,c} = V_{R,c,cyl} = t_{PD,c,exp}\, A_c = f_2(h_c) \tag{2.19}$$

It should be noted that Eq. (2.18) and Eq. (2.19) are still functions depending on the cut height h_c. In Fig. 2.10 the actual considered cut height is denoted as h_c while other alternative cut heights are denoted as $h_{c,alt,i}$. There are these cells, which are truncated close to the bottom and those, which are truncated just at the cell head. So the inner cell volume $V_{R,c}$ can differ from relatively large to rather small. The area A_c in contrast has a maximum at the half cell height and becomes smaller the more h_c increases its distance from the half cell height. This fact is essential with regard to Eq. (2.18). It can be shown that cells with a large h_c do have a large volume $V_{R,c}$ but a small cutting area A_c tending towards zero, whereas low cut cells have both parameters relatively small. Hence, the penetration depth $t_{PD,c,exp}$ does not increase linearly but exponentially with increasing h_c. In terms of the resin cylinder it would mean that the cylinder becomes more and more thinner and longer being attended by a larger penetration depth. The result is a higher weighting of shortly truncated cells in comparison to those having less volume left. Assuming the existence of cells showing all different possible cut heights with the same probability, the mean value $t_{PD,exp}$ is gained by writing in integral notation as follows:

$$t_{PD,exp} = \frac{1}{b-a} \int_a^b f_1(h_c)\, dh_c \tag{2.20}$$

The limits of the integral a and b shall be set in a way that the interval of the integral covers the entire inner volume of the cell. In Nickel's spherical cell that is from $a = t_{sph}$ to $b = 2\,R_c - t_{sph}$.

For the presented spherical cell model this approach has been proofed of being physically accurate due to the consideration of the higher resin volume in shortly truncated cells. However, during research the question came up, why to chose such an approach because when looking only at the actual penetration depth dimension towards the inner of the core (that equals the dimension of h_c), the inner volume of each truncated cell does not seem to play a big role. The intuitive way instead is to assume all cells being half-filled with resin. This condition is fulfilled when calculating $t_{PD,lin}$ by the mean value of the simple linear function:

$$g(h_c) = t_{PD,c,lin} = h_c - t_{sph} \tag{2.21}$$

When assuming each cell of being truncated at half inner cell height $\frac{h_{Cell,in}}{2}$, $t_{PD,lin}$ can be obtained in general as follows:

$$t_{PD,lin} = \frac{h_{Cell,in}}{2} \tag{2.22}$$

Both the exponential and the simple linear approach on penetration depth have been investigated with regard to the applicability on balsa wood cells. The only cell types, which are considered to affect the penetration depth are the ray cells and the fiber cells. For applying Nickel's approach the defined cell geometries are used to determine the inner resin volume $V_{R,c}$ and the cutting area A_c of those cells depending on a cut height h_c. The penetration depth is then gained by using Eq. (2.20).

In detail this approach and especially the derivation of the function $f_1(h_c$ and its integration for each cell both vertically and laterally are quite complicated. Thus, the focus will now be on the results and their plausibility. It could be shown that the usage of the exponential approach does not deliver plausible values for the fiber cells. Assuming a total fiber cell length of $L_f = 650\,\mu\text{m}$ and an average cell end height $h_{end,f} = 70\,\mu\text{m}$ leads to an average penetration depth of $t_{PD,exp} = 1315.5\,\mu\text{m}$. The balsa's nominal apparent density here is $\rho_C = 148\,\frac{\text{kg}}{\text{m}^3}$. This example shows that the overweighting of fiber cells with a lager resin volume is not plausible because the penetration depth extends the total cell length more than twofold. The reason is the pointed cell end, more precisely its converge ratio. The exponential approach leads to expectable values of about $t_{PD,exp} = 450\,\mu\text{m}$ when sizing down the cell end height to $10\,\mu\text{m}$. But as seen on the SEM micrographs (Fig. 2.5) this is much too short to come close to physical reality. Regarding the lateral penetration depth the results from exponential and linear approach are somewhat equal. For the ray cells both approaches show similar values due to the smaller inner cell volume of the rays compared to the fibers.

In conclusion the decision was made to prefer the simple linear approach when calculating the average penetration depth in all directions. The contributing amount of each cell type (rays and fibers) is taken into account with regard to their area fractions. The model further offers the option to switch between Nickel's approach and the simple linear approach.

2.3.3 Smearing Method

One way to unite the material properties of a multi-phase medium mathematically is the so-called smearing method. The word "smearing" means the idea of gaining one homogeneous continuum out of two or more continua by simply adding the different properties after weighting them according to the medium's volume fraction [3].

Hence, applying this method requires the definition of a total volume that contains the volumes of the different mediums. A total volume V_{tot} being set together by the volumes V_i of the single mediums is assumed.

$$V_{tot} = \sum_{i=1}^{k} V_i \tag{2.23}$$

The material property ξ_{sm} for the smeared continuum shall be determined. Accordingly, the non-smeared properties of the single mediums are denoted as ξ_i. The smeared property is then calculated as follows:

$$\xi_{sm} = \sum_{i=1}^{k} n_i \, \xi_i \tag{2.24}$$

The weighting factors n_i are the single mediums' volume fractions:

$$n_i = \frac{V_i}{V_{tot}} \tag{2.25}$$

In the following section, the smearing method is applied both for the density/mass calculation and the stiffness calculation of the resin-infused balsa wood core. With respect to the applicability of the smearing method, the definition of a representative volume element (RVE) is necessary. A RVE is the smallest element of a larger structure, that represents the larger structure as a whole. The structure to be investigated in this case is the whole balsa wooden core plate, infused by resin. Of course, the dimensions of the core plate may be arbitrary, so the total volume has to be represented by a RVE. Here, the contoured structure of the balsa plate is beneficial. The balsa plate is subdivided into many single blocks, which are separated by longitudinal and transversal slits. Those slits are filled with resin during the resin infusion process. A RVE, that contains one balsa block and its surrounding resin, is suitable for applying the smearing method.

Figure 2.11 illustrates how the RVE is gained. Here, the marked volume V_{Core} is the volume of the dry balsa core without any resin, whereas the surrounding volume V_{Resin} is assumed to be the volume that is filled up with resin. The face sheets are not included in the RVE. They shall not be part of the smearing as it is shown here. Instead their properties are calculated with established methods like the CLT and depending on the

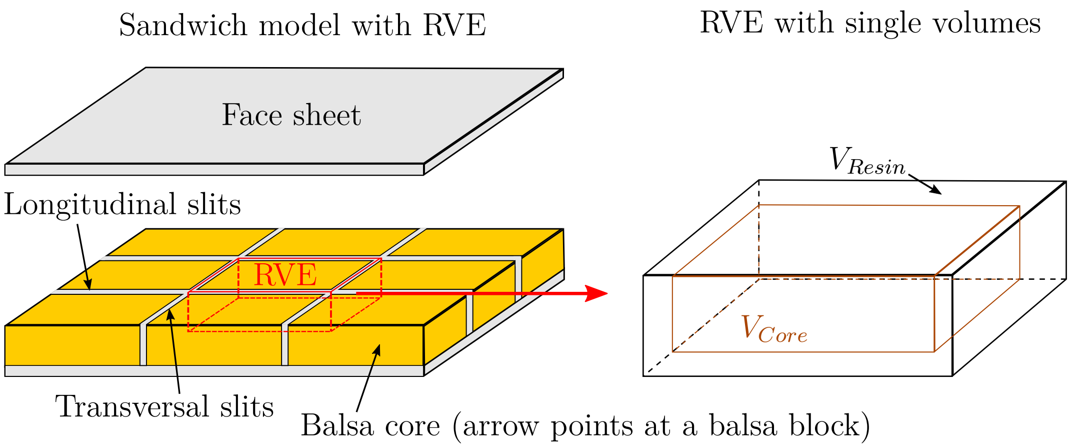

Figure 2.11: RVE of the resin-infused balsa plate

fiber volume fraction of each layer. Nevertheless there is a vertical part of V_{Resin} above the dry core volume. This part represents the resin, which penetrates the truncated cells along the balsa core's surface in vertical direction. The resin, which penetrates laterally, is included in the slits' volumes.

2.4 Application of the Smearing Method

In the previous section the smearing method has been explained and the RVE is determined in principle. This section deals with the application of the smearing method regarding the calculation of mass and stiffnesses of the resin-infused balsa wood core as it is performed in the sandwich model. Mass and stiffness determination are the both main aims of the model. But for deriving both approaches, the RVE has to be specified differently. In the following two subsections those specified RVEs are presented. Furthermore, the final model equations are derived in detail.

At this point it is important to mention that the equations, which are derived in this section, are only valid for the balsa core, whose surface cells and slits are filled with resin. The face sheets are not included as they are implemented separately using established calculation methods.

In general, for specifying the dimensions of the RVE, the model bases on one essential assumption. It is assumed that the RVE's total dimensions equal those of a dry balsa block within the contoured plate. The reason for that assumption is that practically, when having a look at the dry plate before infusion, the slits do not have a certain width because they are cut partially with a sharp knife and then broken off, instead of being sawed. Hence, in ideal circumstances, there is no loss of material. But experiments show that the balsa blocks seem to shrink during the infusion and curing process and here also the wood moisture is relevant as it will be shown in Chap. 4. Additionally, the single blocks are held together by a glass-fiber fabric. So for the RVE, the blocks do shrink while staying on their initial positions. The slits do widen accordingly to the blocks' shrinkage plus a so-called zero opening of 0.2 mm. The zero opening shall describe a mean slit opening resulting by a non-planar positioning (not exactly planar) of the contoured balsa plate before infusion. Together with minimal material losses during cutting and handling of the plate, a zero slit opening is not avoidable in practice.

The chosen RVE in general is taken from Nickel [3, pp. 7-16] and further modified in order to meet the physical structure of balsa wood. Hence, the derived smearing model for the infused balsa wood core and all derivations for mass and stiffnesses do follow the general ideas from Nickel. The modification is done by implementing the different cell geometries in order to determine the penetration depth and in the first place by considering the vessel cells as the largest balsa wood cell type when deriving the equation for the smeared mass and the stiffness equations.

2.4.1 Calculation of Mass

Besides the already shown geometrical approach for the determination of the total core mass, the smearing method delivers a different approach. The aim is to gain a smeared density according to the underlying RVE. Additionally, the total resulting volume $V_{Plate,res}$ of the balsa wood plate after infusion is needed. The calculation of that volume is done by performing some corrections on the plate's geometry with regard to wood moisture, the exposure to vacuum, the curing process of the resin-hardener mixture, some additional shrinkage that has been observed experimentally and lastly the trimming of the plate as desired. These core plate geometry corrections do all base on experimental results, which are stated in Chap. 4 and will not be further explained within this subsection. After the total resulting geometry of the resin-filled plate has been determined, the mass is calculated by multiplying the smeared density by the resulting plate volume.

Essential for determining the smeared density is the definition of the used RVE. Furthermore, some assumptions have to be made to justify the choice of the RVE. Figure 2.12 shows the chosen RVE for the purpose of density smearing.

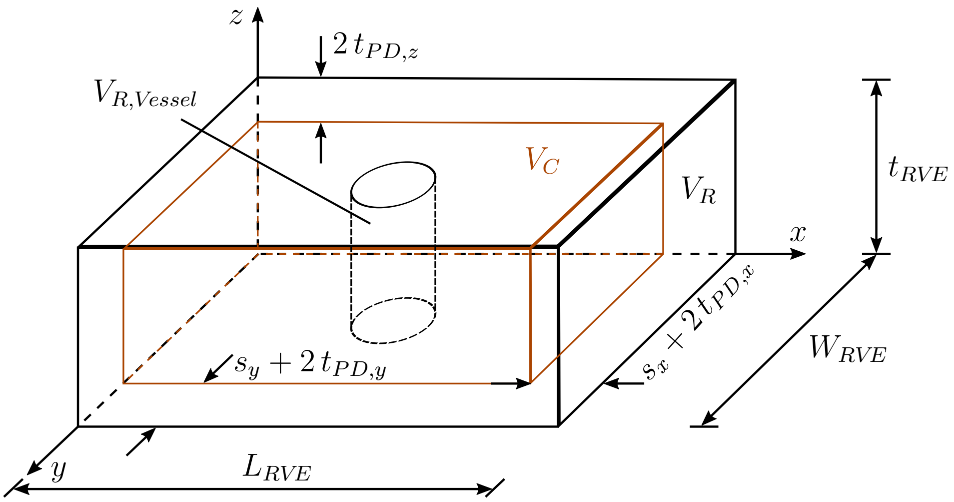

Figure 2.12: RVE for the smearing of density

The depicted RVE consists of two different volumes, the dry core volume V_C and the resin volume V_R. The volume element considers the resin uptake of all three basic cell types along the surfaces of the balsa wood blocks. By implementing the penetration depth t_{PD} both vertically and laterally, the truncated fibers and rays are represented in taking up the resin during infusion. Hence, the cell walls are neglected. In addition the slits are represented by their widths s_x and s_y.

The volume $V_{R,Vessel}$ also belongs to the resin volume V_R, but is named separately to highlight its consideration. The vessel cells usually are distributed arbitrarily across the balsa block surface. In order to simplify the issue, the vessels' area fraction is used and applied to the surface area of one balsa block. Thus all the vessels are treated as one large vessel cell. So with regard to the total vessel volume, it is assumed to be no difference. Using the volume fraction and accordingly the area fraction from Table 2.1, the vessel volume and vessel area per block (per RVE) are gained. Thus, the volume $V_{R,Vessel}$ equals:

$$V_{R,Vessel} = V_{Vessel/RVE} - 2\,A_{Vessel/RVE}\,t_{PD,z} \tag{2.26}$$

With respect to the assumptions and definitions mentioned above, the two volumes V_C and V_R are calculated as follows:

$$V_C = \left(\left(L_{RVE} - s_x - 2\, t_{PD,x} \right) \left(W_{RVE} - s_y - 2\, t_{PD,y} \right) \left(t_{RVE} - 2\, t_{PD,z} \right) \right) - V_{R,Vessel} \tag{2.27}$$

$$V_R = V_{RVE} - V_C = L_{RVE}\, W_{RVE}\, t_{RVE} - V_C \tag{2.28}$$

After the two volumes are determined, the volume fractions n_C and n_R are obtained via Eq. (2.25) with $V_{tot} = V_{RVE}$. The smeared density ρ_{tot} is now gained by applying the smearing equation.

$$\rho_{sm} = \sum_{i=1}^{k} n_i\, \rho_i = n_C\, \rho_C + n_R\, \rho_R \tag{2.29}$$

By applying the smearing method the pure balsa plate and the penetrated resin have been investigated so far. However the model does not neglect the glass-fiber fabric, which holds the single balsa blocks together. The ratio of fiber mass to resin mass is assumed to be 50 %. Further the fabric's mass per unit area is known. The mass of the infused glass-fiber fabric is obtained by using the following equation.

$$m_{Glassfiber,infused} = 2 \left(\frac{m}{A} \right)_{fabric} A_{Plate,res} \tag{2.30}$$

Finally, as already mentioned the smeared mass of the resulting resin-infused core plate is determined with the simple mass-density relation plus the mass of the infused glass-fiber fabric:

$$m_{Plate,res} = \rho_{sm}\, V_{Plate,res} + m_{Glassfiber,infused} \tag{2.31}$$

2.4.2 Calculation of Stiffnesses

This subsection deals with the calculation of in-plane and out-of-plane stiffness moduli of the resin-infused core. As mentioned before, this calculation is based on a different RVE than the mass calculation. The reason is that summarizing all resin-filled vessel cells (resin pillars) by one centered resin-filled cylindrical pillar would result in a mechanically inappropriate solution of the issue. Important here is that the resin pillars are distributed equally across the dry core's surface. The underlying RVE is illustrated in Fig. 2.13.

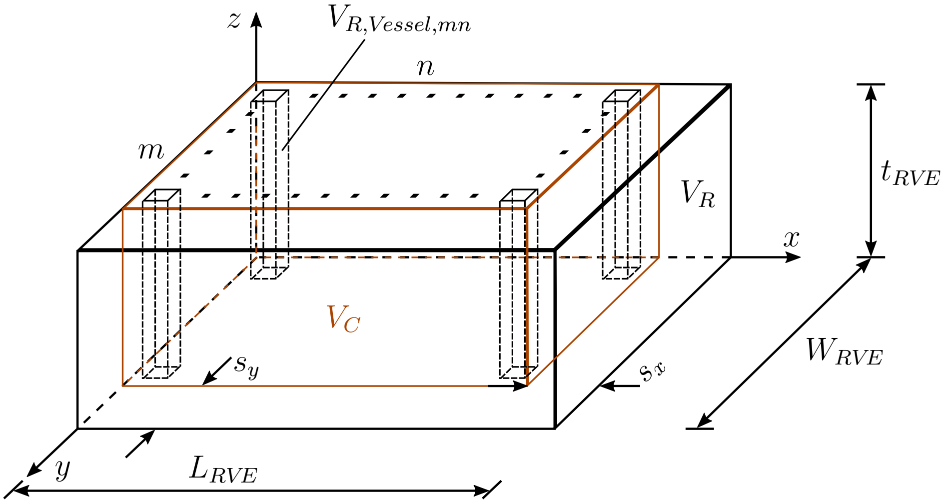

Figure 2.13: RVE for the smearing of stiffnesses

The RVE for the stiffnesses looks quite different in some aspects compared to the one in Fig. 2.12. At first, the single cylindrical pillar is substituted for an arbitrary number of quadratic shaped pillars, which represent the elliptical vessel cells. So here, the elliptical shape is simplified by introducing quadratic pillars having the edge length a. The pillars are arranged in a rectangular pattern. The model allows the customization of that pattern by choosing arbitrarily the number of pillars in y-direction as m and the number of pillars in x-direction as n. However, the decision on what values are set as an input for the calculation should be reasonable. A reasonable choice can be made after having calculated roughly the total number N of vessel cells per balsa block using the area fraction and equal cell geometries of all vessels. Then m and n are chosen in that way that the distance b_x between the pillars in x-direction and the distance b_y between the pillars in y-direction are the same or at least close to each other.

Another major difference in comparison to the RVE for density smearing is that there is no penetration depth t_{PD}. Hence, the resin that penetrates the truncated balsa wood cells is neglected and not represented by the resin volume V_R. The reason is the same as already stated by Nickel for the rigid foam model [3]. Due to the fact, that the balsa cell volumes are continuously separated by their cell walls, the resulting resin structures are assumed to be not capable of carrying any loads. Furthermore, the vertical penetration depth is very small compared to t_{RVE}, while the lateral penetration depth is very small compared to s_x or s_y. So the resin volume V_R does only represent the slits and the vessel cells, fully filled with resin.

The RVE shall now be investigated in order to explain the derivation of the stiffnesses. Figure 2.14 gives a more detailed view for deriving the equation for the Young's modulus E_x in x-direction.

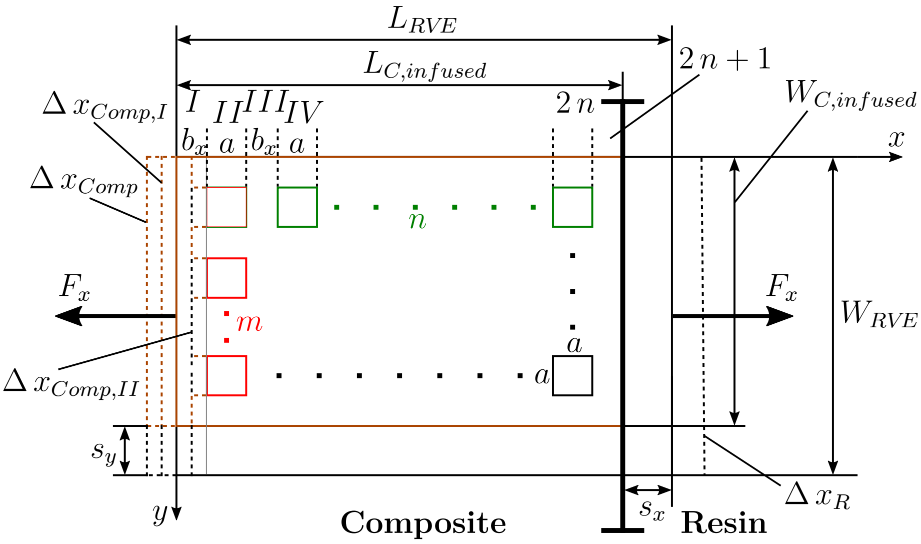

Figure 2.14: RVE in xy-plane

For the purpose of the determination of E_x and E_y analogously, the xy-plane of the RVE is depicted. The total vessel number N is gained by multiplying m by n.

$$N = m\,n \tag{2.32}$$

The resin filled squared pillars shall have the dimension $a\,\mathrm{x}\,a$. The edge length a is gained by using the total area of the vessel cells per RVE and distribute it to the single squared pillars.

$$a = \sqrt{\frac{1}{N}\,A_{Vessel/RVE}} \tag{2.33}$$

The space between the pillars is denominated as b_x and b_y respectively. Equal spaces along the dry core's surface leads to the following equations:

$$b_x = \frac{L_{C,infused} - n\,a}{(n+1)} \tag{2.34}$$

$$b_y = \frac{W_{C,infused} - m\,a}{(m+1)} \tag{2.35}$$

The infused core lengths are determined by subtracting the relative slit width from the total RVE dimension.

$$L_{C,infused} = L_{RVE} - s_x \tag{2.36}$$

$$W_{C,infused} = W_{RVE} - s_y \tag{2.37}$$

The applied Forces F_x lead to strains on both sides of the RVE. The seen RVE plane is subdivided into a pure resin part, here represented by the slit width s_x, and a composite part consisting of dry core and resin slit. For the total deformation in x-direction the deformation $\Delta\, x_{Comp}$ of the composite part and the deformation $\Delta\, x_R$ of the resin part are added.

$$\Delta\, x_{tot} = \Delta\, x_R + \Delta\, x_{Comp} \tag{2.38}$$

Now it is assumed that the composite's deformation results from adding together the single deformations of the columns I, II, III, IV to column $2\,n+1$. Those columns (or rows for the y-direction) alternately contain the resin pillars or they do not. By presuming linear elastic material behaviour and the strain definition $\varepsilon = \frac{\Delta\, x}{x}$ the resin part's deformation and the single columns' deformations are obtained as follows:

$$\Delta\, x_R = \varepsilon_{R,x}\, s_x \tag{2.39}$$

$$\Delta\, x_{Comp,I} = \varepsilon_{Comp,I,x}\, b_x \tag{2.40}$$

$$\Delta\, x_{Comp,II} = \varepsilon_{Comp,II,x}\, a \tag{2.41}$$

The deformations for the remaining columns III to $2\,n+1$ are gained in the same way, each column alternating by its width b_x or a. The entire formulation of Eq. (2.38) with all deformations is:

$$\Delta\, x_{tot} = \Delta\, x_R + \Delta\, x_{Comp,I} + \Delta\, x_{Comp,II} + \cdots + \Delta\, x_{Comp,2\,n+1} \tag{2.42}$$

By implementing the stress-strain relation $\sigma = E\,\varepsilon$ (Hooke's law for linear elastic material behaviour), Eq. (2.42) can be rewritten.

$$\underbrace{\frac{\sigma_x}{E_x}\, L_{RVE}}_{\Delta\, x_{tot}} = \underbrace{\frac{\sigma_x}{E_R}\, s_x + \frac{\sigma_x}{E_{Comp,I,x}}\, b_x + \frac{\sigma_x}{E_{Comp,II,x}}\, a + \cdots + \frac{\sigma_x}{E_{Comp,2\,n+1,x}}\, b_x}_{A_x} \tag{2.43}$$

The right part of the equation shall further be named as A_x. Now, the smearing method is applied to calculate the Young's moduli of the composite part using the single phase modulus of the resin E_R and the dry core modulus $E_{C,x}$. From Fig. 2.14 it is apparent that all columns denoted with an odd index number share the same cross-section without resin pillars, whereas all even numbered columns do share the same cross-section including the resin pillars. When determining the volume fraction of columns in the composite part, it is sufficient to just take the cross-sectional length fraction into account because thickness and column width are the same. Hence, there are two different Young's moduli to be determined via smearing: one for the odd numbered columns with the width b_x and one for the even numbered columns with the width a.

$$E_{Comp,Odd,x} = \frac{s_y}{W_{RVE}}\,E_R + \left(1 - \frac{s_y}{W_{RVE}}\right)\,E_{C,x} \tag{2.44}$$

$$E_{Comp,Even,x} = \frac{s_y + m\,a}{W_{RVE}}\,E_R + \left(1 - \frac{s_y + m\,a}{W_{RVE}}\right)\,E_{C,x} \tag{2.45}$$

Due to the fact that all cross-sections share the same load F_x as well as the same cross-sectional area, the tensile stress σ_x is the same in each deformation summand. Therefore it can be reduced. The term A_x is now further summarized to $A_{x,red}$:

$$A_{x,red} = \frac{1}{E_R}\,s_x + (n+1)\,\frac{1}{E_{Comp,Odd,x}}\,b_x + n\,\frac{1}{E_{Comp,Even,x}}\,a \tag{2.46}$$

Finally, the modulus E_x is gained with respect to Eq. (2.43).

$$E_x = \frac{L_{RVE}}{A_{x,red}} \tag{2.47}$$

In order to determine the modulus E_y the derivation is done analogously. The analogue derivation leads to the following equation:

$$\underbrace{\frac{\sigma_y}{E_y}\,W_{RVE}}_{\Delta\,y_{tot}} = \underbrace{\frac{\sigma_y}{E_R}\,s_y + \frac{\sigma_y}{E_{Comp,I,y}}\,b_y + \frac{\sigma_y}{E_{Comp,II,y}}\,a + \cdots + \frac{\sigma_y}{E_{Comp,2\,m+1,y}}\,b_y}_{A_y} \tag{2.48}$$

The smeared moduli are gained respectively.

$$E_{Comp,Odd,y} = \frac{s_x}{L_{RVE}}\,E_R + \left(1 - \frac{s_x}{L_{RVE}}\right)\,E_{C,y} \tag{2.49}$$

$$E_{Comp,Even,y} = \frac{s_x + n\,a}{L_{RVE}}\,E_R + \left(1 - \frac{s_x + n\,a}{L_{RVE}}\right)\,E_{C,y} \tag{2.50}$$

It can be summarized:

$$A_{y,red} = \frac{1}{E_R}\, s_y + (m+1)\, \frac{1}{E_{Comp,Odd,y}}\, b_y + m\, \frac{1}{E_{Comp,Even,y}}\, a \tag{2.51}$$

And consequently E_y is obtained.

$$E_y = \frac{W_{RVE}}{A_{y,red}} \tag{2.52}$$

The remaining stiffness in z-direction can be derived in a similar way. When having a look at Fig. 2.14 again, it is imaginable to apply a Force in z-direction pointing out of the depicted plane. The resulting deformation in z-direction affects the entire cross-sectional area of the RVE. Hence, there is only one smeared Young's modulus $E_z = E_{Comp,z}$. The required volume fraction of the dry core is represented by its area fraction, here denoted as A_z.

$$A_z = \frac{L_{C,infused}\, W_{C,infused} - A_{Vessel/RVE}}{L_{RVE}\, W_{RVE}} \tag{2.53}$$

Implementing this formulation, E_z is determined as follows:

$$E_z = E_{Comp,z} = A_z\, E_{C,z} + (1 - A_z)\, E_R \tag{2.54}$$

After the Young's moduli the derivation of the shear moduli shall be done with reference to another view on the RVE. A shear force leads to an out-of-plane deformation, further denoted as the vertical displacement w. Figure 2.15 illustrates the deformed situation.

In general the derivation is done in the equivalent way, as it is done for the Young's moduli. The definition for the total number of resin filled pillars N is the same as well as for a, b_x and b_y. Hence, these operands are calculated according to Eqs. (2.32 to 2.37).

The RVE is again subdivided into a resin part and a composite part. Equivalent to Eq. (2.38), the total vertical displacement is gained by adding the vertical displacement of both parts.

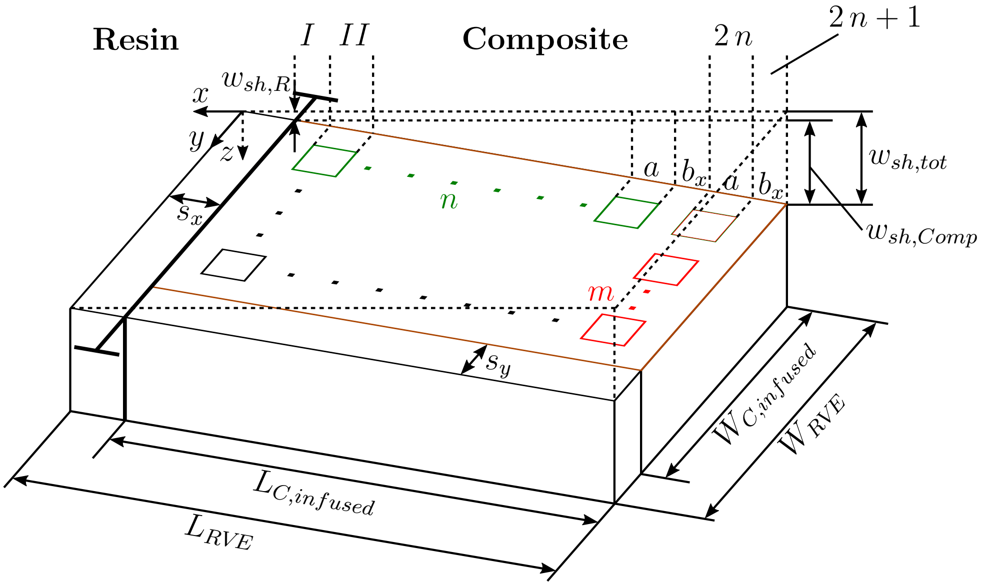

Figure 2.15: Shear deformation of RVE in xz-plane

$$w_{sh,tot,xz} = w_{sh,R,xz} + w_{sh,Comp,xz} \tag{2.55}$$

Again, the composite's deformation $w_{sh,Comp,xz}$ is simply consisting of the vertical displacements of each column, which are added together. For the next step it is assumed that the shear strain γ is very small, so that the lengths L_{RVE} and $L_{C,infused}$ are used as initially defined and there is no displacement in x-direction depending on the vertical displacement ($\frac{\partial u}{\partial z} = 0$). Therefore, the relation $\gamma = \frac{\partial w}{\partial x}$ is used in order to determine both the resin part displacement and the columns' partial vertical displacements.

$$w_{sh,R,xz} = \gamma_{R,xz}\, s_x \tag{2.56}$$

$$w_{sh,Comp,I,xz} = \gamma_{Comp,I,xz}\, b_x \tag{2.57}$$

$$w_{sh,Comp,II,xz} = \gamma_{Comp,II,xz}\, a \tag{2.58}$$

The aim of this derivation is to obtain an equation for the shear modulus G_{xz}. Thus, the single vertical displacements have to consist of an appropriate expression. The shear strain γ can be substituted by the ratio of shear stress τ to the shear modulus G ($\gamma = \frac{\tau}{G}$). By using this relation, Eq. (2.55) is consequently rewritten as:

$$\underbrace{\frac{\tau_{xz}}{G_{xz}}\,L_{RVE}}_{w_{sh,tot,xz}} = \underbrace{\frac{\tau_{xz}}{G_R}\,s_x + \frac{\tau_{xz}}{G_{Comp,I,xz}}\,b_x + \frac{\tau_{xz}}{G_{Comp,II,xz}}\,a + \cdots + \frac{\tau_{xz}}{G_{Comp,2\,n+1,xz}}\,b_x}_{A_{xz}} \tag{2.59}$$

The shear moduli, which represent the columns of the composite part of the RVE, are summarized as already presented before into one smeared modulus for the odd numbered columns and one smeared modulus for the even numbered columns.

$$G_{Comp,Odd,xz} = \frac{s_y}{W_{RVE}}\,G_R + \left(1 - \frac{s_y}{W_{RVE}}\right)G_{C,xz} \tag{2.60}$$

$$G_{Comp,Even,xz} = \frac{s_y + m\,a}{W_{RVE}}\,G_R + \left(1 - \frac{s_y + m\,a}{W_{RVE}}\right)G_{C,xz} \tag{2.61}$$

Since τ_{xz} is constant within all cross-sectional areas, Eq. (2.59) is devided by τ_{xz} in order to define $A_{xz,red}$ as:

$$A_{xz,red} = \frac{1}{G_R}\,s_x + (n+1)\,\frac{1}{G_{Comp,Odd,xz}}\,b_x + n\,\frac{1}{G_{Comp,Even,xz}}\,a \tag{2.62}$$

This leads to the final formulation for G_{xz}:

$$G_{xz} = \frac{L_{RVE}}{A_{xz,red}} \tag{2.63}$$

The derivation of G_{yz} is done completely in the analogue way as for G_{xz}. Hence, the necessary equations are given below without further annotations.

$$G_{Comp,Odd,yz} = \frac{s_x}{L_{RVE}}\, G_R + \left(1 - \frac{s_x}{L_{RVE}}\right) G_{C,yz} \tag{2.64}$$

$$G_{Comp,Even,yz} = \frac{s_x + n\, a}{L_{RVE}}\, G_R + \left(1 - \frac{s_x + n\, a}{L_{RVE}}\right) G_{C,yz} \tag{2.65}$$

$$A_{yz,red} = \frac{1}{G_R}\, s_y + (m+1)\, \frac{1}{G_{Comp,Odd,yz}}\, b_y + m\, \frac{1}{G_{Comp,Even,yz}}\, a \tag{2.66}$$

$$G_{yz} = \frac{W_{RVE}}{A_{yz,red}} \tag{2.67}$$

Now the out-of-plane shear stiffnesses have been derived. This subsection closes with the derivation of the final equations for the smeared in-plane stiffnesses G_{xy} and G_{yx}. Basically the approach is equal to the out-of-plane shear deformation. Instead of the vertical displacement w_{sh} there are the horizontal displacements u_{sh} and v_{sh}. The shear deformation causing the shear strain γ_{xy} equals the displacement v_{sh} in y-direction, whereas u_{sh} represents the displacement in x-direction causing the shear strain γ_{yx}. Like done before, the derivation is firstly shown exemplarily for one of the two mentioned moduli, here G_{xy}. The RVE is deformed in the way shown in Fig. 2.16.

The operands N, a, b_x and b_y do not change, even though the squared shape of the resin-filled pillars is sheared, too. So the resin pillars' edge length a is still gained by using Eq. (2.33). It is presumed that the total displacement $v_{sh,tot}$ is set together of the resin part's displacement $v_{sh,R}$ plus the composite part's displacement $v_{sh,Comp}$.

$$v_{sh,tot} = v_{sh,R} + v_{sh,Comp} \tag{2.68}$$

Considering a very small shear strain γ_{xy} without partial strain nonparallel to the y-axis ($\frac{\partial u}{\partial y} = 0$), both $v_{sh,R}$ and the single column summands of column I to $2\,n+1$ can be rewritten into the familiar form:

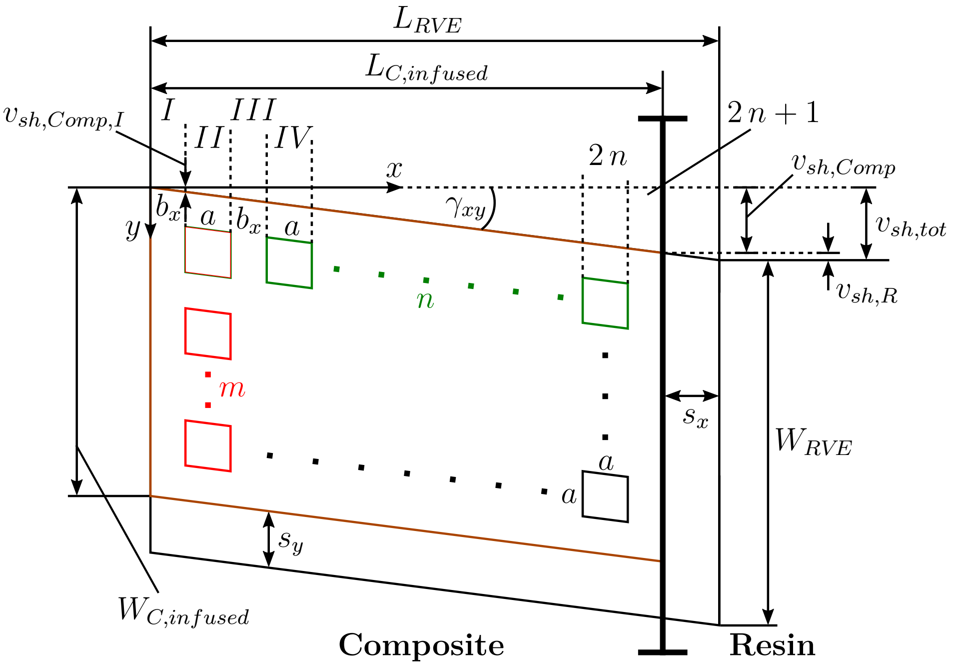

Figure 2.16: Shear deformation of RVE in xy-plane (here: y-displacement)

$$v_{sh,R} = \gamma_{R,xy}\, s_x \tag{2.69}$$

$$v_{sh,Comp,I} = \gamma_{Comp,I,xy}\, b_x \tag{2.70}$$

$$v_{sh,Comp,II} = \gamma_{Comp,II,xy}\, a \tag{2.71}$$

The shear modulus G is introduced by the relation $\gamma = \frac{\tau}{G}$, which is inserted into Eq. (2.68).

$$\underbrace{\frac{\tau_{xy}}{G_{xy}}\, L_{RVE}}_{v_{sh,tot}} = \underbrace{\frac{\tau_{xy}}{G_R}\, s_x + \frac{\tau_{xy}}{G_{Comp,I,xy}}\, b_x + \frac{\tau_{xy}}{G_{Comp,II,xy}}\, a + \cdots + \frac{\tau_{xy}}{G_{Comp,2\,n+1,xy}}\, b_x}_{A_{xy}} \tag{2.72}$$

The even and odd numbered shear moduli are now summarized as already known:

$$G_{Comp,Odd,xy} = \frac{s_y}{W_{RVE}}\, G_R + \left(1 - \frac{s_y}{W_{RVE}}\right) G_{C,xy} \tag{2.73}$$

$$G_{Comp,Even,xy} = \frac{s_y + m\, a}{W_{RVE}}\, G_R + \left(1 - \frac{s_y + m\, a}{W_{RVE}}\right) G_{C,xy} \tag{2.74}$$

With the reduced right side term of Eq. (2.72) the final equation for the shear modulus G_{xy} is obtained.

$$A_{xy,red} = \frac{1}{G_R}\, s_x + (n+1)\, \frac{1}{G_{Comp,Odd,xy}}\, b_x + n\, \frac{1}{G_{Comp,Even,xy}}\, a \tag{2.75}$$

$$G_{xy} = \frac{L_{RVE}}{A_{xy,red}} \tag{2.76}$$

The shear strain γ_{yx} is described by a shear displacement u_{sh} in x-direction. The derivation of the shear modulus G_{yx} is equivalent to the derivation for G_{xy}. To avoid further repetition, the elementary equations are stated but not commented.

$$G_{Comp,Odd,yx} = \frac{s_x}{L_{RVE}}\, G_R + \left(1 - \frac{s_x}{L_{RVE}}\right) G_{C,yx} \tag{2.77}$$

$$G_{Comp,Even,yx} = \frac{s_x + n\, a}{L_{RVE}}\, G_R + \left(1 - \frac{s_x + n\, a}{L_{RVE}}\right) G_{C,yx} \tag{2.78}$$

$$A_{yx,red} = \frac{1}{G_R}\, s_y + (m+1)\, \frac{1}{G_{Comp,Odd,yx}}\, b_y + m\, \frac{1}{G_{Comp,Even,yx}}\, a \tag{2.79}$$

$$G_{yx} = \frac{W_{RVE}}{A_{yx,red}} \tag{2.80}$$

Before this subsection comes to an end, one thing is important to mention. Due to the fact that the blocks of the contoured balsa core are rectangular, the respective dry core volume of the RVE has a rectangular shape, too. That means that the shown derivations deliver results for the stiffness moduli, which explicitly depend on the underlying coordinate directions, even if the pure balsa structure does not show up differences. For example, there is no actual difference in the balsa structure when comparing x-direction and y-direction. That may seem somewhat counterintuitive, but it is the most exact geometry implementation that takes the resin uptake into account. In addition, the slit widths s_x and s_y are not necessarily the same due to different direction dependent shrinkage of the single balsa blocks, caused by the loss of moisture or resin hardening. In other words, the equivalent stiffnesses would be equal in the case that $m = n$, $L_{RVE} = W_{RVE}$ and $s_x = s_y$. These parameters can be chosen arbitrarily within the model. However, the actual geometry of the balsa blocks shows remarkable influence on the calculated stiffnesses.

The mechanical constants (Young's moduli E_C and shear moduli G_C) of the pure balsa core material, which are used in the smearing equations are calculated by equations given by Gibson and Ashby for wood in general [11, p. 418]. Since the balsa plate is set together by many pieces of arbitrary rotational orientation, the tangential and radial constant components in the xy-plane are unified in the analytical model by implementing the respective mean value. The used equations include the so-called relative density ρ_{rel}. It is defined as the ratio of the density of the core material ρ_C and the density of the pure solid cell wall material ρ_s.

$$\rho_{rel} = \frac{\rho_C}{\rho_s} \tag{2.81}$$

The used solid cell wall density is defined as $\rho_s = 1500\,\frac{\mathrm{kg}}{\mathrm{m}^3}$. This value is assumed to be close to the cell wall material density of all types of wood [12].

2.5 Classical Laminate Theory (CLT)

This section deals with the derivation of the classical laminate theory (CLT) as described by Schürmann [16, pp. 205-228, pp. 323-340]. The CLT offers a calculation methodology, which allows the determination of the stiffnesses of a multi-layer composite plate. That means that the flexural properties of a composite plate, which consists of several unidirectional (UD) layers, can be investigated by adding the stiffnesses of each single UD layer. The main aim of the CLT is the set-up of an equation or rather a system of equations that describe the elastic behaviour of the total composite plate.

Before deriving this system of equations, some assumptions have to be stated, which lie behind the theory [16]:

- there are no acting mass forces (like weight or inertia forces)
- the plate shows rigid behaviour against shear loads and shear displacements, so that the core of a sandwich plate does not show elastic behaviour, when being exposed to shear loads (only consideration of bending moments resulting by a shear load Q)
- plane stress is assumed (multi-layer composite is thin-walled)
- the material shows ideal linear elastic behaviour (Hooke's law is applicable)
- the element thickness (plate thickness) is constant
- the multi-layer composite consists of several UD layers (UD layer as homogeneous continuum)
- all single UD layers are connected perfectly to each other (no slipping between the layers, no adhesive layers)

In a first step two operands are defined by dividing the acting force N and the acting moment M by the width b. In vector notation[16]:

$$\underline{\hat{n}} = \frac{\hat{N}}{b} = \begin{bmatrix} \hat{n}_x \\ \hat{n}_y \\ \hat{n}_{xy} \end{bmatrix} \tag{2.82}$$

$$\underline{\hat{m}} = \frac{\hat{M}}{b} = \begin{bmatrix} \hat{m}_x \\ \hat{m}_y \\ \hat{m}_{xy} \end{bmatrix} \tag{2.83}$$

The symbol "^" declares that the marked operands refer to the total multi-layer composite plate. The plane stress condition is shown on an example multi-layer composite element in Fig. 2.17:

Regarding the shown forces and moments, it is stated that $\hat{n}_{xy} = \hat{n}_{yx}$ as well as $\hat{m}_{xy} = \hat{m}_{yx}$. For the purpose of calculations, which will be shown later in this section, a reference plane has to be defined. Usually it is defined as the composite's mid-plane. The layer numbering begins with $k = 1$ at the bottom layer and counts up to the top layer $k = n$. In order to define the thickness of each single layer, the z-coordinates are introduced in dependence on the reference plane.

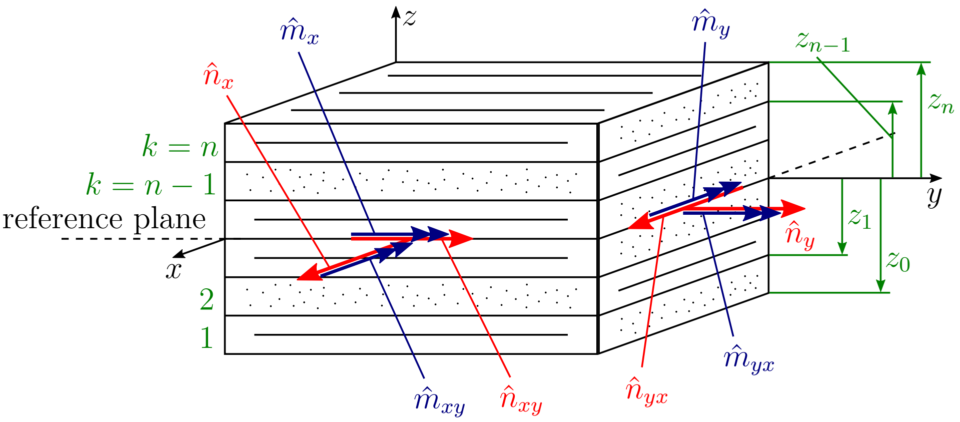

Figure 2.17: Plane stress on multi-layer composite and layer numbering

Due to the fact, that the indication of moments may differ depending on the underlying literature, it is important to define, how the indication is meant for this thesis. A moment is indicated in the way, that the index marks the normal direction of the plane, in which those stresses occur, which are caused by the moment. For example the moment $\hat{m}_x$ causes stresses in the composite's plane with the normal in x-direction. This would be the yz-plane.

In the CLT each layer is attributed with the so-called reduced UD layer stiffness matrix $\underline{\underline{Q}}$. Assuming plane stress condition, Hooke's law is applied for the single UD layer as follows [16]:

$$\underline{\sigma} = \underline{\underline{Q}}\,\underline{\varepsilon}$$

$$\underbrace{\begin{bmatrix} \sigma_{\parallel} \\ \sigma_{\perp} \\ \tau_{\perp\parallel} \end{bmatrix}}_{\underline{\sigma}} = \underbrace{\begin{bmatrix} \frac{E_{\parallel}}{1-\nu_{\perp\parallel}\,\nu_{\parallel\perp}} & \frac{\nu_{\parallel\perp}\,E_{\parallel}}{1-\nu_{\perp\parallel}\,\nu_{\parallel\perp}} & 0 \\ \frac{\nu_{\perp\parallel}\,E_{\perp}}{1-\nu_{\perp\parallel}\,\nu_{\parallel\perp}} & \frac{E_{\perp}}{1-\nu_{\perp\parallel}\,\nu_{\parallel\perp}} & 0 \\ 0 & 0 & G_{\perp\parallel} \end{bmatrix}}_{\underline{\underline{Q}}} \underbrace{\begin{bmatrix} \varepsilon_{\parallel} \\ \varepsilon_{\perp} \\ \gamma_{\perp\parallel} \end{bmatrix}}_{\underline{\varepsilon}} \tag{2.84}$$

Equation (2.84) is written in the local $\parallel\perp$-coordinate system as the indication shows. The index $\parallel$ indicates the direction parallel to the longitudinal fiber direction, where as the index $\perp$ indicates the direction perpendicular to the longitudinal fiber direction. The single layers of the multi-layer composite consist of fibers, which are unidirectional. So each layer k is defined by its fiber angle α. Usually, for a multi-layer composite the stacking sequence of the single layers is not homogeneous. In fact, the different UD layers do differ in terms of their fiber angle α to enable a certain strength in predefined directions. Hence, the single UD layers have their own local $\|\perp$-coordinate systems. Therefore, the $\underline{\underline{Q}}$-matrix has to be transformed using transformation matrices, here defined as $\underline{\underline{T}}_1$ and $\underline{\underline{T}}_2$. Equation (2.87) makes sure that all local coordinate systems are turned into one global coordinate system. Those Q-elements are marked with an overline [16].

$$\underline{\underline{T}}_1 = \begin{bmatrix} \cos^2\alpha & \sin^2\alpha & -\sin 2\alpha \\ \sin^2\alpha & \cos^2\alpha & \sin 2\alpha \\ 0.5\,\sin 2\alpha & -0.5\,\sin 2\alpha & \cos 2\alpha \end{bmatrix} \tag{2.85}$$

$$\underline{\underline{T}}_2 = \begin{bmatrix} \cos^2\alpha & \sin^2\alpha & 0.5\,\sin 2\alpha \\ \sin^2\alpha & \cos^2\alpha & -0.5\,\sin 2\alpha \\ -\sin 2\alpha & \sin 2\alpha & \cos 2\alpha \end{bmatrix} \tag{2.86}$$

$$\underline{\underline{\overline{Q}}} = \underline{\underline{T}}_1\,\underline{\underline{Q}}\,\underline{\underline{T}}_2 \tag{2.87}$$

Now, to begin with the derivation of the total multi-layer composite stiffness matrix $\underline{\underline{M}}$, the forces $\underline{n}_k$ and moments $\underline{m}_k$ are added together to form the total operands [16].

$$\underline{\hat{n}} = \sum_{k=1}^{n} \underline{n}_k \tag{2.88}$$

$$\underline{\hat{m}} = \sum_{k=1}^{n} \underline{m}_k \tag{2.89}$$

Considering the kinematic relation for strain $\underline{\hat{\varepsilon}} = \underline{\varepsilon}_0 + z\,\underline{\kappa}_0$ (index 0: depending on reference plane) and after applying Hooke's law and solving the occuring integrals like Schürmann did [16], the following equations are gained [16]:

$$\underline{\hat{n}} = \sum_{k=1}^{n} \left(\underline{\underline{\overline{Q}}}_k \left(z_k - z_{k-1}\right) \varepsilon_0 + \underline{\underline{\overline{Q}}}_k \frac{1}{2} \left(z_k^2 - z_{k-1}^2\right) \kappa_0 \right) \tag{2.90}$$

$$\underline{\hat{m}} = \sum_{k=1}^{n} \left(\underline{\underline{\overline{Q}}}_k \frac{1}{2} \left(z_k^2 - z_{k-1}^2\right) \varepsilon_0 + \underline{\underline{\overline{Q}}}_k \frac{1}{3} \left(z_k^3 - z_{k-1}^3\right) \kappa_0 \right) \tag{2.91}$$

These two equations can be transferred into the main system of equations, which is delivered by the CLT. It contains the total stiffness matrix $\underline{\underline{M}}$. The corresponding units are shown below.

$$\begin{gathered}\begin{bmatrix} \underline{\hat{n}} \\ \underline{\hat{m}} \end{bmatrix} = \underbrace{\begin{bmatrix} \underline{\underline{A}} & \underline{\underline{B}} \\ \underline{\underline{B}} & \underline{\underline{D}} \end{bmatrix}}_{\underline{\underline{M}}} \begin{bmatrix} \underline{\varepsilon} \\ \underline{\kappa} \end{bmatrix}_0 \\ \begin{bmatrix} \frac{\mathrm{N}}{\mathrm{mm}} \\ \mathrm{N} \end{bmatrix} = \begin{bmatrix} \frac{\mathrm{N}}{\mathrm{mm}} & \mathrm{N} \\ \mathrm{N} & \mathrm{N\,mm} \end{bmatrix} \begin{bmatrix} - \\ \frac{1}{\mathrm{mm}} \end{bmatrix}\end{gathered} \tag{2.92}$$

The matrix $\underline{\underline{M}}$ with the dimension [6 x 6], also called ABD-matrix, can be subdivided into its sub-matrices $\underline{\underline{A}}$, $\underline{\underline{D}}$ and $\underline{\underline{B}}$. Each of these sub-matrices has the dimension [3 x 3]. The elements of the in-plane stiffness matrix $\underline{\underline{A}}$ are calculated by summing up the reduced UD layer stiffnesses multiplied by their thicknesses [16].

$$A_{ij} = \sum_{k=1}^{n} \overline{Q}_{ij,k} \left(z_k - z_{k-1}\right) = \sum_{k=1}^{n} \overline{Q}_{ij,k}\, t_k \tag{2.93}$$

In order to gain the bending stiffness matrix $\underline{\underline{D}}$, it is necessary to consider the layers' z-coordinates [16].

$$D_{ij} = \frac{1}{3} \sum_{k=1}^{n} \overline{Q}_{ij,k} \left(z_k^3 - z_{k-1}^3\right) = \sum_{k=1}^{n} \overline{Q}_{ij,k} \left(\frac{t_k^3}{12} + t_k \left(z_k - \frac{t_k}{2} \right)^2 \right) \tag{2.94}$$

The $\underline{\underline{B}}$-matrix is also called the coupling matrix. Its elements couple the in-plane forces $\underline{\hat{n}}$ with the out-of-plane curvatures $\underline{\kappa}_0$ and the out-of-plane moments $\underline{\hat{m}}$ with the in-plane stresses $\underline{\varepsilon}_0$ [16].

$$B_{ij} = \frac{1}{2}\sum_{k=1}^{n} \overline{Q}_{ij,k}\,(z_k^2 - z_{k-1}^2) = \sum_{k=1}^{n} \overline{Q}_{ij,k}\, t_k \left(z_k - \frac{t_k}{2}\right) \tag{2.95}$$

In case of a symmetrical build-up of the multi-layer composite plate, the elements of the matrix $\underline{\underline{B}}$ equal zero. Hence, there is no coupling of in-plane and out-of-plane operands. Due to the fact that the sandwich specimens used in this work are symmetrical, the elements B_{ij} are supposed to equal zero.

Further, there should be a closer look at the elements A_{ij} and D_{ij} to examine how they are interpreted. For the case that all elements B_{ij} equal zero, the following correlations can be stated:

$$\underline{\hat{n}} = \underline{\underline{A}}\,\underline{\varepsilon} \tag{2.96}$$

$$\underline{\hat{m}} = \underline{\underline{D}}\,\underline{\kappa} \tag{2.97}$$

With respect to the simple relation $\sigma = \frac{F}{A}$ and considering Eq. (2.96) it is possible to formulate:

$$\underline{\sigma} = \frac{1}{t_{sw}}\,\frac{\underline{\hat{N}}}{b} = \frac{1}{t_{sw}}\,\underline{\hat{n}} = \underbrace{\frac{1}{t_{sw}}\,\underline{\underline{A}}}_{\underline{\underline{E}}}\,\underline{\varepsilon} \tag{2.98}$$

In addition, with $\kappa = -w''$ [16] and with respect to the bending line equation (see Eq. (2.112) in Subsect. 2.7.2), Eq. (2.97) can be rewritten as:

$$\underline{M} = \underbrace{b\,\underline{\underline{D}}}_{\underline{\underline{EI}}}\,(-\underline{w''}) \tag{2.99}$$

Consequently, the elements A_{ij} and D_{ij} can be interpreted by transforming them to the in-plane elements E_{ij} and the bending stiffnesses $B = E_{ij}\,I$.

$$E_{ij} = \frac{1}{t_{sw}}\,A_{ij} \tag{2.100}$$

$$B = E_{ij}\,I = b\,D_{ij} \tag{2.101}$$

That means that the elements of the multi-layer composite stiffness sub-matrix $\underline{\underline{A}}$ and $\underline{\underline{D}}$ are not directly interpreted as in-plane stiffnesses or bending stiffnesses. The required transformations as derived above are in agreement with the corresponding units.

Nevertheless, it is important to mention the fact that all elements of the total stiffness matrix $\underline{\underline{M}}$ are calculated using the reduced matrix $\underline{\underline{Q}}$. Hence, their transversal contraction is restricted due to plane stress conditions. In order to obtain the elements without restricted transversal contraction, a further transformation is needed using the elements of the inverse matrix $\underline{\underline{M}}^{-1}$.

$$A_{ij,not\,restricted} = \frac{1}{A_{ij}^{-1}} \tag{2.102}$$

$$D_{ij,not\,restricted} = \frac{1}{D_{ij}^{-1}} \tag{2.103}$$

$$B_{ij,not\,restricted} = \frac{1}{B_{ij}^{-1}} \tag{2.104}$$

Finally, by inserting Eq. (2.102) in Eq. (2.100) and Eq. (2.103) in Eq. (2.101) the engineer constants of the sandwich are obtained:

$$E_{ij,sw} = \frac{1}{t_{sw}}\,\frac{1}{A_{ij}^{-1}} \tag{2.105}$$

$$B_{sw} = E_{ij,sw}\,I_{sw} = b\,\frac{1}{D_{ij}^{-1}} \tag{2.106}$$

For the purpose of comparison with results from the four point bending test, the bending stiffness elements D_{ij} are important. The element D_{11} represents the bending stiffness B_x, i.e. the stiffness, which counteracts against a moment acting about the plate's y-axis causing strains in x-direction.

The CLT calculations, more precisely the calculation of the total stiffness matrix $\underline{\underline{M}}$ and its inverse matrix $\underline{\underline{M}}^{-1}$ and the engineer constants are integrated in the stiffness calculation model.

2.6 Four Point Bending Test Configuration

As the bending stiffness is one of the most critical stiffnesses considering the possible buckling failure modes of sandwich panels, the decision was made to perform four point bending tests according to engineer standards. The main advantage of a four point bending configuration is the fact that the bending moment between the loading bars is constant, while the acting shear force equals zero. That allows a simple calculative application of the bending line theory.

To perform a test, which guarantees a satisfying level of reproducibility and comparability, the four point bending test is usually done according to a suitable engineer standard. There are two engineer standards that come into consideration when performing a four point bending test. On the one hand there is the German standard DIN 53 293 published by the Deutsches Institut für Normung (DIN) [17] and on the other hand there is the ASTM C393/C393M by the American Society for Testing and Materials (ASTM) [18]. Both standards and the mechanical theory behind a four point bending test are described in the following subsection.

2.6.1 Engineer Standards and Load Distribution

Both the DIN 53 293 and the ASTM C393/C393M are suitable for a four point loading configuration with sandwich beam constructions. But the standards differ in their guidelines concerning the test apparatus configuration and the test specimen's geometries. For the choice of the standard used for this thesis, former experience on four point testing with sandwich specimens was the determining factor. While the DIN 53 293 gives several strict specifications on the specimen's geometry and the distances of the test apparatus, the ASTM C393/C393M is much less strict.

In the DIN 53 293 the sandwich specimen is defined by the length L, the width b and the total thickness h. The sandwich's cross-section itself is defined by h accordingly, the face sheet thickness t and the core thickness c. Here it is assumed that the sandwich is symmetrical, so that upper and lower face sheets are equally thick. In addition, d is defined as the distance between the center planes of the face sheets.

$$d = c + t = \frac{h + c}{2} \tag{2.107}$$

In an early point in time of this thesis, the decision had to be made, what thickness the balsa wooden core plates shall have. At this point the only references available was the work from Nickel [3] on the one side and on the other side there were experimental data from former four point bending tests that have been performed at the IWES. The sandwich specimens that have been used back then, had balsa cores with a thickness of 25 mm. Nickel used core thicknesses between 10 mm and 25 mm for the foam core specimens. Hence, for the reason of comparability, balsa plates with a thickness of 25.4 mm (1 in.) and 12.7 mm ($\frac{1}{2}$ in.) have been ordered within the scope of this thesis. Also with respect to the former sandwich specimens, the face sheets were roughly estimated to be 2.0 mm to 2.5 mm in thickness each.

The length L of the sandwich specimen is strictly given in the DIN 53 293 in dependency of the thickness h as follows:

$$L = 24\,h \tag{2.108}$$

For a sandwich with a thickness of $h = 30$ mm the length would be 720 mm. The full dimensions of the ordered balsa plate were 1220 x 610 mm. So a specimen length larger than 610 mm would result in a large amount of cut-off when manufacturing. Additionally, there might occur restrictions concerning the available space inside the apparatus that is used for performing the four point bending test.

Furthermore, the usage of the equations given in the DIN 53 293 standard is only valid under two more conditions, which concern the ratio of thicknesses d and t and the bending stiffnesses of face sheet and core material. However, these requirements are not mentioned in this thesis, because they are not the leading point in the decision making of what standard is used.

Regarding the argumentation above, the decision was made to use the ASTM C393/C393M-16 standard (further named as ASTM C393). The addition "-16" refers to the published version of this standard as this was the active standard at the time of preparing the bending experiment. The later published "-20" version was not consulted.

The ASTM C393 is suitable both for a three point loading configuration and for a four point loading configuration. The three point loading is denominated as standard configuration while the four point loading is non-standard. The dimensions of the test apparatus are defined by the support span length S and the load span length L. Assuming a centered build-up, the corresponding distance between support bar and loading bar is called D_{SL}. The standard defines two different variants of configurations: quarter-span and third-span. Table 2.2 shows the data for all mentioned configurations.

Table 2.2: Loading configurations according to ASTM C393

	Configuration	$\boldsymbol{S}$	$\boldsymbol{L}$	$\boldsymbol{D_{SL}}$
Standard	3-Point (Mid-Span)	150 mm	0.0	$S/2$
Non-Standard	4-Point (Quarter-Span)	S	$S/2$	$S/4$
	4-Point (Third-Span)	S	$S/3$	$S/3$

The support span length S can be chosen arbitrarily in a suitable way as long as no application of the equations given in the standard is required. In the present case of this thesis, it is not planned to use any of the given equations for later calculations. Otherwise the following condition has to be fulfilled:

$$S \leq \frac{2\,k\,\sigma\,t}{F_S} + L \tag{2.109}$$

where: k = facing strength factor to ensure core failure (recommend $k = 0.75$)
σ = expected facing ultimate strength [MPa]
t = face sheet thickness [mm]
F_S = estimated core shear strength [MPa]

Another requirement for using the standard's equations is that the face sheets have the same thickness and modulus (symmetrical sandwich) and that the face sheet thickness t is small in relation to the core thickness c.

$$\frac{t}{c} \leq 0.1 \tag{2.110}$$

As opposed to the DIN standard, the ASTM C393 does not require a specimen length, which is in dependence on the specimen's thickness. Instead, for the non-standard configurations, the specimen length a shall be equal to either $S + 50\,\mathrm{mm}$ or $S + \frac{d}{2}$, whatever is greater. Here d is the total sandwich thickness. The face sheet thickness t and the core thickness c are defined as in the DIN 53 293. The specimen width b shall be not less than $2\,d$ and not exceed $6\,d$. In addition b shall not be greater than $\frac{a}{2}$. If the core consists of countable elements, like blocks in the case of a contoured balsa core with slits, the specimen's width shall contain at least three times the dimensions of an element.

The test configuration and the distribution of the occurring mechanical loads are shown in Fig. 2.18.

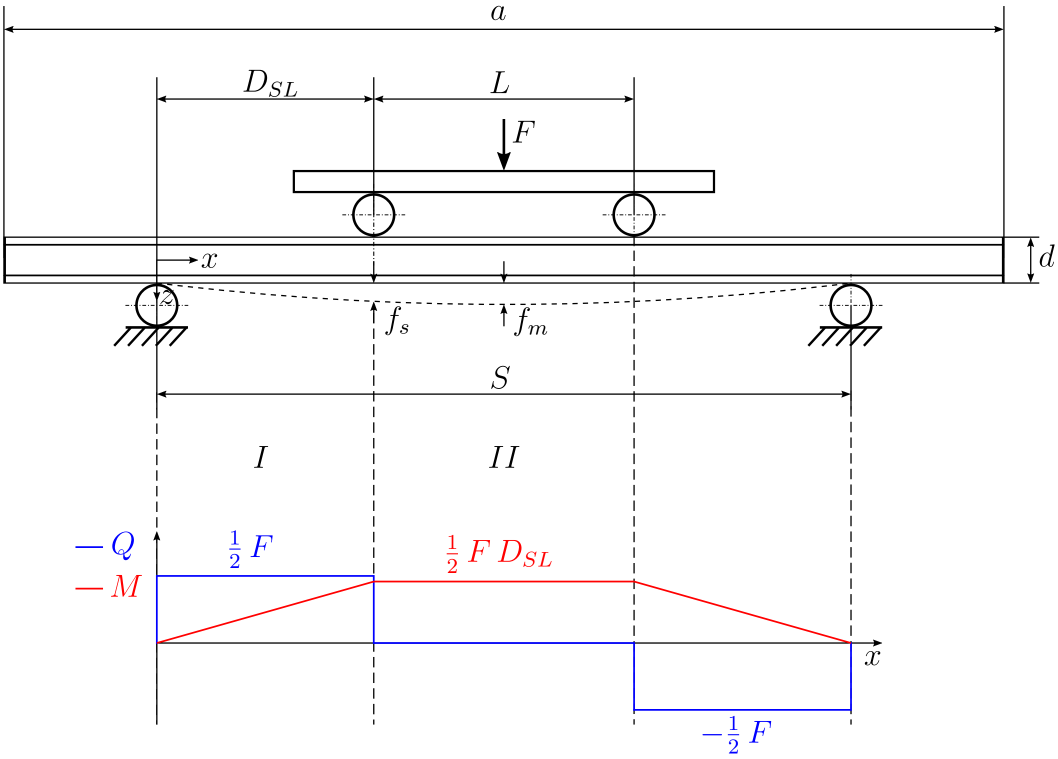

Figure 2.18: Test build-up according to ASTM C393

The acting forces on the sandwich specimen when a loading force F is applied in the center between the loading bars do all have the absolute value $\frac{1}{2}\,F$. The negative forces at the positions of the support bars counter those, which act in positive direction at the loading bar positions. This results in the given distribution of shear force Q (blue) and bending moment M (red). It can be distinguished between region I and region II. For applying the bending line theory, the bending moment distribution $M_y(x)$ in region II is needed. Additionally, the vertical displacements f_s (at support bar position) and f_m (at mid-beam position) are measured.

2.6.2 Bending Line Theory

The bending line theory is used in order to determine the bending stiffness from the data gained in the four point bending test. More precisely, it is possible to calculate the bending stiffness that leads to strains in the specimen's longitudinal direction. For the reason of terminology, in this subsection the specimen shall be named as beam to match with literature of the topic bending line. The longitudinal direction is defined as the beam's x-direction. Hence, the basic equation of the bending line is given in dependence of the longitudinal variable x [19].

$$\frac{w''(x)}{(1+w'(x)^2)^{\frac{3}{2}}} = -\frac{M_y(x)}{E_x(x)\,I_y(x)} \tag{2.111}$$

Equation (2.111) is not linear, but it can be approximated with the assumption that the vertical displacement $w(x)$ of the beam is small enough to keep the slope $w'(x) \ll 1$. This assumption equals a linear elastic behaviour of the beam. What remains is Eq. (2.112), the 2nd order differential equation of the bending line [3].

$$w''(x) = -\frac{M_y(x)}{E_x(x)\,I_y(x)} = -\frac{M_y(x)}{B_x(x)} \tag{2.112}$$

Here, $w''(x)$ is the curvature, $M_y(x)$ is the acting bending moment and $E_x(x)\,I_y(x)$ can be combined to the bending stiffness $B_x(x)$ at the longitudinal position x. $E_x(x)$ is the Young's modulus in x-direction and $I_y(x)$ is the area moment of inertia for a bending rotation relative to the beam's y-axis.

With reference to the former depicted moment distribution (Fig. 2.18) it is now possible to define the bending moment distributions for region II as follows:

$$M_{II}(x) = \frac{1}{2}\, F\, D_{SL} \qquad \text{with } x \in [D_{SL}, \frac{S}{2}] \tag{2.113}$$

After insertion into Eq. (2.112), the curvature $w''_{II}(x)$ can be integrated in order to gain the slope $w'_{II}(x)$ and the measurable vertical displacement $w_{II}(x)$ with the integration constants C_1 and C_2.

$$w''_{II}(x) = -\frac{M_{II}(x)}{B_x(x)} = -\frac{F\, D_{SL}}{2\, B_x(x)} \tag{2.114}$$

$$w'_{II}(x) = -\frac{F\, D_{SL}}{2\, B_x(x)}\, x + C_1 \tag{2.115}$$

$$w_{II}(x) = -\frac{F\, D_{SL}}{4\, B_x(x)}\, x^2 + C_1\, x + C_2 \tag{2.116}$$

The integration constants C_1 and C_2 can be calculated by having a look on the boundary conditions within the four point bending configuration. Firstly, it is obvious that the slope $w'_{II}(x)$ at the beam's mid-position equals zero:

$$w'_{II}(x = \frac{S}{2}) = 0 \quad \Leftrightarrow \quad C_1 = \frac{F\, D_{SL}\, S}{4\, B_x(x)} \tag{2.117}$$

C_2 can be obtained by assuming that $w_{II}(x = D_{SL}) = w_I(x = D_{SL})$. For doing so, $w_I(x)$ has to be derived in the equivalent way as $w_{II}(x)$ is derived in Eqs. (2.113 to 2.116). For the sake of simplicity, those steps are not described in detail in this thesis. Instead, the derivation can be looked up in the work from Nickel, which this thesis is based on [3, pp. 29,30]. The integration constant C_2 finally is calculated as:

$$C_2 = -\frac{F\, D_{SL}^3}{12\, B_x(x)} \tag{2.118}$$

Hence, the complete equation for $w_{II}(x)$ can be written down inserting C_1 and C_2.

$$w_{II}(x) = -\frac{F\, D_{SL}}{4\, B_x(x)}\, x^2 + \frac{F\, D_{SL}\, S}{4\, B_x(x)}\, x - \frac{F\, D_{SL}^3}{12\, B_x(x)} \tag{2.119}$$

By inserting the measured vertical displacements f_s or f_m for $w_{II}(x)$ and the corresponding force F at the positions $x = D_{SL}$ or $x = \frac{S}{2}$ it is now possible to determine the bending stiffness $B_x(x)$.

$$B_x(x) = -\frac{D_{SL}\, F\, (3\, x\, (x - S) + D_{SL}^2)}{12\, w_{II}(x)} \tag{2.120}$$

3 Experimental Methods and Procedures

This chapter at first deals with the methods and procedures of the experiments that have been done in order to investigate the balsa wood material behaviour. These experiments all contribute to the resulting plate geometry in the model's calculation process. Furthermore pure balsa wood plates are infused without glass-fiber layers for the purpose of validation of the model's mass calculation methods. The chapter closes with detailed explanations concerning all relevant aspects of the four point bending tests. Besides the test apparatus configuration that includes the manufacturing process of the specimens and the derivation of the equations used to determine the specimens' stiffnesses with the data gained from the bending tests.

3.1 Research on Balsa Wood Material Behaviour

Balsa wood is a naturally grown material that reacts on the environmental conditions, which it is exposed to. Hence, its geometry is depending to a relatively large extend on parameters like wood moisture or on the curing effect of resin that surrounds or penetrates the balsa wood core. Additionally, the vacuum leads to further reduction of moisture content, so there has been an experiment, too.

3.1.1 Wood Moisture

Balsa wood in general is a material that is preferred amongst others due to its low density. This low density originates from the high amount of empty cell volume inside the wood. In Table 2.1 the solid fraction of each cell type can be seen. It shows that each cell of MD balsa for example has a solid fraction, which does not exceed a value of roughly 10 %. So the majority of volume inside a piece of balsa wood is empty. However, with regard to the moisture content, it is the solid cell wall material, which is capable of containing water even at moisture contents that appear in industrial environments.

The moisture content of wood is usually measured in mass percent. That means that the measured value in % represents the fraction of water mass that is bound inside the wood relative to the dry mass of the wood. Wood that has been lumbered recently can have moisture contents of 100 % or higher. In this case the cell walls and the inner cell lumens are completely filled with water. For industrial subsequent treatment the wood is dried. Balsa wood plates show moisture contents of about 10 %. At such low moisture content the cell lumens are not filled with water any more. But the remaining water is bound inside the cell wall material and affects significantly its geometry. The cell walls then behave more or less like a sponge. Thus, the wood experiences shrinkage and swelling, that depends on its moisture content on the one side and on the wood's orientation on the other side, because wood generally shrinks and swells differently regarding axial, tangential and radial direction. The geometry change in axial direction (vertical balsa plate direction z) is assumed to be neglectably small [20].

The shrinkage/swelling behaviour of balsa wood is investigated by performing an experiment. For this experiment a large number of balsa blocks is individually separated from a contoured balsa wood plate (nominal contoured block geometry: 50.8 x 25.4 mm). Then their density is predetermined by weighting each block and setting the block's weight in relation to the nominal block volume. From the gained list of blocks 30 blocks are chosen as samples for the experiment. Within the scope of this thesis balsa plates of two different thicknesses have been ordered from Gaugler & Lutz, 25.4 mm (1 in.) and 12.7 mm ($\frac{1}{2}$ in.). One half of the 30 samples has the thickness 25.4 mm, the other half is 12.7 mm thick. In addition, each 15 samples are divided into the three different density classes ρ_L (low density), ρ_M (medium density) and ρ_H (high density) depending on what range of densities is on hand. The used balsa wood plates both are of type BALTEK SB.100 with an apparent nominal density of 148 $\frac{\mathrm{kg}}{\mathrm{m}^3}$ and a minimum sheet density of 136 $\frac{\mathrm{kg}}{\mathrm{m}^3}$ (manufacturer's data). After predetermination of the densities, all blocks are oven-dried at 45 °C for at least 16 h. Then their length, width and thickness is measured and the samples are weighted again. Thus the actual air-dry density is determined.

Table 3.1: Density classes for wood moisture experiment

	$\boldsymbol{\rho_L}$	$\boldsymbol{\rho_M}$	$\boldsymbol{\rho_H}$
Samples			
ρ_{min} $[\frac{\text{kg}}{\text{m}^3}]$	78.95	120.38	145.94
ρ_{max} $[\frac{\text{kg}}{\text{m}^3}]$	120.85	149.18	179.32
Defined ranges			
ρ $[\frac{\text{kg}}{\text{m}^3}]$	<120	120 to 150	>150

Table 3.1 shows the minimum and maximum of the determined air-dry density values in each density class. According to these values the range for the experiment is defined. So five samples of the 15 samples per thickness do share one density class.

The dry samples are now exposed to an environment with a constant temperature of 23 °C and a variable relative air humidity. This is done by placing the samples into a climate chamber. The relative air humidity is set to 50 % before bringing in the balsa samples. Then after 2 h of exposure time the air humidity is increased by steps of +10 % up to finally 80 %. Between every step of +10 % air humidity, 2 h elapse. The 15 samples are subdivided into five groups of three samples, each group containing samples of each density class. While one group of samples stays inside the climate chamber continuously throughout all steps of air humidity, each group of the remaining four is put inside the climate chamber at one of the four steps (air humidity: 50 %, 60 %, 70 %, 80 %). Before each step, i.e. after 2 h of exposure time the samples are weighted and their geometry and wood moisture content is measured.

For the measurement of the wood moisture content, the material moisture measuring device T510 from the company Trotec GmbH is used. The moisture is measured according to the resistance measurement method. A measuring current is generated within the material via electrodes, which are inserted into the wood. Depending on the water content the material's resistance and its conductivity changes. The Trotec T510 has an integrated temperature compensation and wood type correction including balsa wood. The absolute error in mass percent is depending on the actual measured moisture. It is 0.8 % for a measured moisture of 0 to 5 %, 0.2 % for a measured moisture of 6 to 30 % and 0.1 % for a measured moisture of 31 to 100 %. The measurement of block length, width and thickness is done with a caliper gauge from the company Mitutoyo having a digital display. The samples' weight is determined using an analytical balance from the company RADWAG. The climate chamber is the model KBF 240, fabricated by BINDER GmbH.

3.1.2 Vacuum

During the VARTM process the balsa core plate is exposed to vacuum for a certain time. This condition is assumed to be another factor that might influence the moisture content and thus the geometry of the balsa blocks. For the investigation of that influence a total number of nine balsa block samples (50.8 x 25.4 mm) is chosen from the separated balsa block samples that have been already used for the moisture content experiment. Three samples each belong to one of the density classes that are introduced in Table 3.1. Two samples out of three have a nominal thickness of 12.7 mm, the third one is 25.4 mm in thickness.

The experiment shall reveal how the vacuum influences the wood moisture content quantitatively over time. It is assumed that the vacuum leads to a remarkable loss of moisture content. That is why the wood moisture content has to be increased at first. Therefore, all nine balsa samples are placed inside the climate chamber first in order to expose them to a relative air humidity of 80 % at a constant temperature of 23 °C. The time duration shall be long enough to ensure a moisture content of about 15 % to make a potential decrease recognizable. With respect to the former performed moisture experiment this are roughly 6 to 8 h. Afterwards, all samples are removed from the climate chamber and put aside for measurements. The measured quantities are length, width, thickness, weight and moisture content. Then the samples are covered by a vacuum film, which is closed like a bag to contain all samples. With a negative pressure of about -0.9 bar to -0.95 bar the vacuum is applied for a duration of 30 min. After this time has elapsed, the samples are removed from the vacuum bag and previously mentioned measurements are repeated. The procedure is done two more times until the samples have been exposed to vacuum for 1.5 h in total.

The measuring instruments are widely the same as used for the previously presented moisture content experiment, but with an exception here. For measuring the width and the thickness of each balsa block (not the length), a spring loaded digital caliper gauge (model: STUDENROTH Hildegard) is used to ensure a more precise determination of the respective lengths by applying constant and reproducible pressure when the gauge gets into contact with the sample. As the gauge's maximum limit is 30 mm the metering range is not sufficiently large to enable the measurement of the length, too.

3.1.3 Resin Infusion and Curing

A third experiment is done to investigate the geometry change of the balsa blocks as part of a large balsa plate. More precisely, the expanding of the slit widths between the balsa blocks during resin infusion and curing process is of interest here. In the first place, the aim is to gain knowledge about to what extend the resin infusion and curing contribute to the total slit width quantitatively. For the model it is assumed that the balsa blocks stay at their individual position while the liquid resin fills the slits and in doing so presses against the lateral surfaces of the balsa blocks. The resin thus widens the minimal open slits. Additionally, former investigation has shown that the resin experiences a chemical volume shrinkage during the curing process when changing from liquid to hardened state [21].

For this experiment, a contoured balsa core plate of type BALTEK SB.100 with a nominal thickness of 25.4 mm and a nominal block size of 50.8 x 25.4 mm is used. This plate is later referred to as plate A as it is used for the validation of the model's mass calculation. In order to assure an air-dry core plate, the plate is oven-dried. An average measured moisture content of about 5 % is intended and finally achieved. After drying, the plate's geometry is measured to 1195 x 402 mm and the plate is also weighed. The aim is to spectate the slits in close-up view during resin infusion and curing. Thus the infusion of the pure core plate is done on a glass plate. The close-up view on a few slits in the middle of the plate is realized by two cameras, which are each equipped with a time-adjustable remote-control release to ensure automatic photography while the resin is impregnating the balsa wood core. Additional photographs are made after the curing process. Then the plate is trimmed and the weight is determined using a balance.

The slit widths are determined by metallic rulers, which are fixed at the bottom side of the glass plate so that they are part of the photographs.

Besides plate A two more balsa plates are purely infused, being referred to as plate B and plate C. In the first place these further resin infusion experiments are done to gain more validation data for the mass calculation methods of the model. However, the fabricated core plates also serve as smaller sized samples, which are suitable for being investigated with an optical microscope. Thus, the slit size is measured on microscopic level with the help of the corresponding software. Before infusion Plate B has a nominal thickness of 25.4 mm and is 561.5 x 257 mm in size, measured with a ruler. Plate C is a thin plate having a nominal thickness of 12.7 mm and a measured size of 559 x 254.5 mm. Nominally the length and width of both plates are the same since they have been cut according to the same block pattern. After the infusion and curing, the excessive hardened resin is removed from the manufactured plates. Finally, the plates are weighed and their geometry is measured with a metallic ruler.

3.2 Four Point Bending Test

In order to gain experimental results for the model validation the sandwich's bending and shear stiffness is determined by performing a four point bending test of the test specimens. This section begins with a brief description of what kind of test apparatus is used to apply the testing machine's load in a correct manner to the specimen. Then the manufacturing of the sandwich specimens, especially the build-up of the face sheet layers, is presented. Furthermore, the actual experimental set-up including the final distances between the support and loading bars and the test procedure is described. The section closes with the derivation of the equations used for the calculation of bending and shear stiffness.

3.2.1 Test Apparatus

The test apparatus for the four point bending test (see Figure 3.2) consists of two separated parts, one upper part and one bottom part. Each part is made of alloy profiles, which are mounted in a proper way to enable the possibility to variably attach the support and loading bars. The bars themselves are single units, each consisting of two rotational bearings and one cylinder. They are fixed to the alloy parts via screws at desired position. The actual support/loading bar again is mounted on the rotational cylinder and thus the apparatus allows free rotational movement of the specimen at the points of loading during the bending test. Since the surface of the bars is in contact to the specimen, rubber pressure pads do cover the contact surfaces. The support's width is large enough to exceed the width of the sandwich specimens. On both the upper and the bottom part a steel profile is mounted where the test apparatus is clamped into the test machine.

3.2.2 Manufacturing and Geometry of Specimens

As the developed model is suitable for plane sandwich plates of arbitrary size, it is evident to perform the bending test using sandwich specimens according to an engineer standard. As explained in Subsect. 2.6.1 for sizing the sandwich specimen the engineer standard ASTM C393/C393M is used.

The specimens are manufactured at IWES. It is reasonable to do a resin infusion for a large sandwich plate at first and to cut it afterwards in the postulated size. The used dry balsa wood plates from Gaugler & Lutz measure in total 760 x 610 mm and 686 x 610 mm. The balsa wood is of type BALTEK SB.100 and the plates both are contoured with a nominal block size of 50.8 x 25.4 mm. The specimens shall cover two different core thicknesses in order to get an idea of how the model's predictions and especially the resin uptake are influenced regarding two plates only differing by their balsa core thickness. For the thin specimens a nominal core thickness of 12.7 mm is used. The larger plate also has the larger thickness of 25.4 mm.

The remaining definition of the face sheet layer stacking sequence is done with regard to former performed flexural beam tests, more precisely four point bending fatigue tests. Within this test series, static bending tests have been done in advance until failure of the sandwich specimens. So the stacking sequence of the glass-fiber layers is chosen in accordance to experience that has been gained by the mentioned static tests to ensure a failure of the specimen with the known testing configuration. Almost all parameters of the experimental set-up are taken from the former experiment, too.

The laminate layer stacking sequence is fully defined by coding the layers of one face sheet as follows:

$$[(0/90)_2/(\pm 45)_2]$$

The codification describes the number of UD layers, their fiber angle α and the stacking sequence of the single layers. In the present case the code, read from left to right, represents the layers being stacked from the bottom to the core plate. So this means that one face sheet begins with two layers of glass-fiber non-crimp fabric, each having one UD layer with a fiber angle of 0° and one UD layer with a fiber angle of 90°. On top of these two fabrics another two layers of non-crimp fabric is placed, this time with ±45° fiber angle. So there are eight UD layers in total per face sheet. The upper face sheet is manufactured symmetrically relative to the core's center plane to ensure a symmetrical sandwich as required in the standard. For all non-crimp fabric layers E-Glass from the company SAERTEX with a mass per unit area of 778 $\frac{\mathrm{g}}{\mathrm{m}^2}$ (see Appendix A). This face sheet layer layout is used for both core thicknesses.

For the resin infusion an infusion resin system consisting of the Epikote$^{\mathrm{TM}}$ Resin MGS RIMR 035C and the Epikure Curing Agent MGS RIMR 037 from HEXION is used (see Appendix B). As far as possible the curing cycle has been adhered to the following steps:

1. infusion at 35 °C
2. curing at 40 °C for 10 h
3. increase in temperature up to 80 °C (rate: 10 °C/h), curing at 80 °C for 7 h
4. cooling at room temperature

After the two sandwich plates have finished curing, the specimen are cut out of the plates. The desired specimen length is taken from the intended to equal 550 mm based on experience from the mention former experiments. The specimens' width is not constant as it depends on the block width (core element width) of the contoured balsa core. At least three core elements are required in width. That is equal to a nominal specimen width of 76.2 mm. However, due to the resin inside the slits between the blocks and the irregular dry block size, the width of the specimens varies. Actually it is important to stick with the three element width regarding the conformity with the symmetry of the specimen's slit pattern.

Figure 3.1 exemplarily shows a thin sandwich specimen.

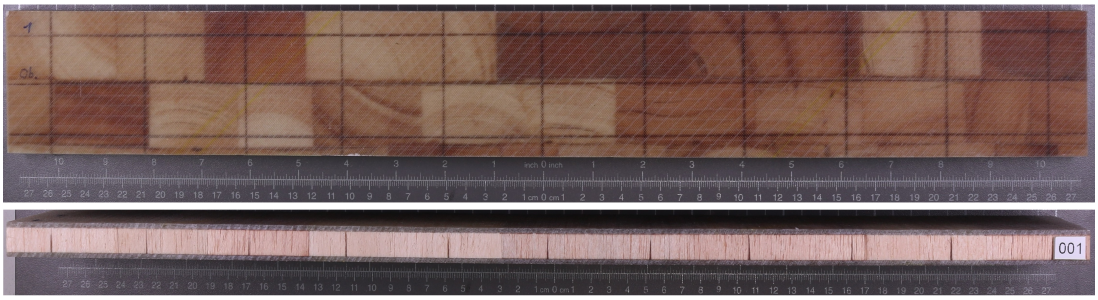

Figure 3.1: Top and side view of a specimen

Eight sandwich specimens are gained out of each plate and their geometry is measured using caliper gauges (Mitutoyo and STUDENROTH Hildegard) and a metallic ruler. Each specimen is weighed. The geometries (length L, width W and thickness t_{sw}) of all 16 specimens are given in Table 3.2.

Table 3.2: Specimens' geometries

	$t_{C,nom}$ [mm]	L [mm]	W [mm]	t_{sw} [mm]
Spec. No.				
1	12.7	550	73.37	17.09
2	12.7	550	73.32	17.05
3	12.7	550	72.19	17.14
4	12.7	550	74.97	17.07
5	12.7	550	72.21	16.99
6	12.7	550	73.06	17.12
7	12.7	550	73.16	17.06
8	12.7	550	73.37	17.19
9	25.4	550	75.44	29.77
10	25.4	550	71.10	29.81
11	25.4	550	72.36	29.91
12	25.4	550	73.40	29.91
13	25.4	550	72.65	29.82
14	25.4	550	72.72	29.68
15	25.4	550	76.37	29.67
16	25.4	550	70.44	29.76

3.2.3 Experimental Set-Up

The experimental set-up that is chosen for the four point bending test can be seen in Fig. 3.2.

The test apparatus is fixed to the test machine. The test machine itself is a bi-axial universal testing machine of type LFV 100 kN, manufactured by Walter + Bai AG. Thus it is able to bring up forces in axial direction up to a nominal force of 100 kN. The chosen distances of the support and loading bars are not in accordance with the engineer standard, since they base on experience from similar sandwich bending tests. Figure 3.3 illustrates the final test configuration for the four point bending test of all specimen.

For applying the bending line theory in order to determine the bending stiffness, it is necessary to measure the vertical displacements at the loading bar position and if desired at mid-beam position. Due to that reason a laser distance sensor is installed on the lower part of the test apparatus pointing at the specimen's lower mid-surface

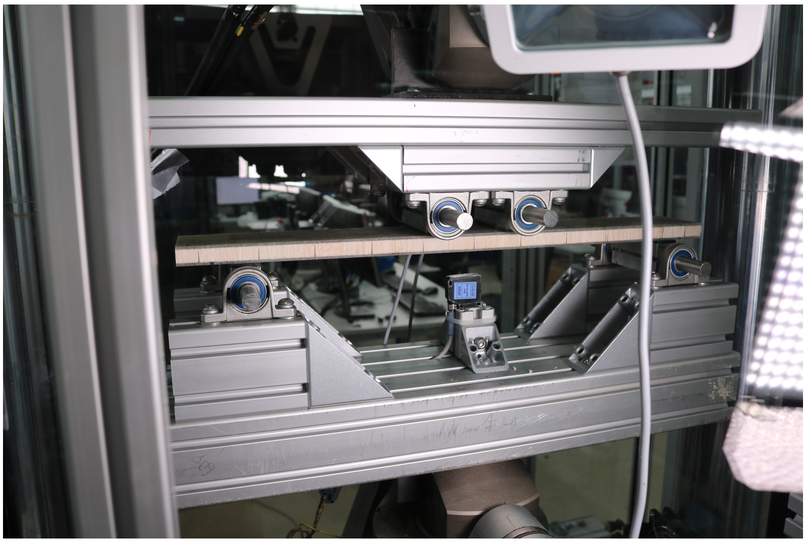

Figure 3.2: Experimental set-up with installed sandwich specimen

position. The measuring range of the laser distance sensor is limited to a certain distance measured from the device's edge. This results in a maximum measurable vertical displacement of 20 mm at mid-beam position. An extension of that limit is not possible since the laser sensor's positioning is restricted with regard to the available free space of the test apparatus.

The vertical displacement at loading bar position is assumed to be equal to the path of the machine's cross head. That machine path is measured by a linear variable differential transformer (LVDT). When applying the bending line theory a high accuracy of the measured vertical displacements is essential as it can influence the calculated bending stiffness significantly. The most accurate way would be a measurement of the vertical displacement along the sandwich beam's mid-plane. Unfortunately that is practically not measurable, so the displacement at the sandwich's surface is taken for the bending line calculation instead. Another error might occur due the resilience of the cross head itself when acting loads on to specimens with high stiffness. This would lead to larger measured vertical distances at loading bar position. Hence, the measured vertical displacement might be corrected.

To ensure the determination of the bending stiffness, the decision has been made to also apply strain gauges both to the upper surface side and the lower surface side of each sandwich specimen, centered at mid-beam position. With the help of the measured strains it is possible to calculate the bending stiffness independent of any influence from the test machine resilience. As the upper surface of the specimen

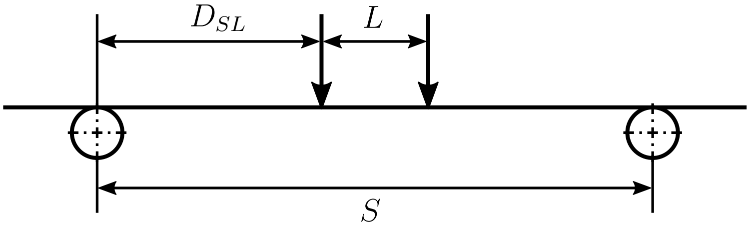

$S = 440\,\text{mm}$
$L = 82\,\text{mm}$
$D_{SL} = 179\,\text{mm}$

Figure 3.3: Test configuration

experiences a compressive force the strain is expected to be negative, whereas the strain gauge at the lower surface is expected to measure positive tensile strains of the same amount.

3.2.4 Test Procedure

Here, the test procedure shall briefly be described for the four point bending test of one sandwich specimen. The test specimen is equipped with the strain gauges as previously described. Then it is installed in centered position onto the test apparatus and the strain gauges are connected. Now the cross head is lowered manually until the rubber pads of the upper half of the test apparatus gets into contact with the specimen's surface. This is done while checking the contact force in order to ensure a zero load position before starting the test. After the positioning of the cross head all measured parameters (load, machine path, mid-beam distance to laser sensor and strains) are zeroed. The test is done path-controlled by holding a standard speed for cross head displacement of $6\,\frac{\text{mm}}{\text{min}}$ according to ASTM C393 [18, p. 5]. Since the laser distance sensor limits the possible vertical beam displacement, the cross head is programmed to stop automatically at a measured machine path of 30 mm and return to home position. In case of specimen failure, the home position is reached via manual input.

3.2.5 Determination of Mass and Stiffnesses

The masses of the sandwich specimens are determined by weighing. Of course this is done before performing the bending test.

There are two different kinds of stiffnesses that are determined by using gained data from the four point bending tests. The first stiffness to be determined is the bending stiffness B_x, defined as stiffness that counteracts against a moment acting about the plate's y-axis causing strains in x-direction. This stiffness is calculated using Eq. (2.120):

$$B_x(x) = -\frac{D_{SL}\,F\,(3\,x\,(x-S)+D_{SL}^2)}{12\,w_{II}(x)} \tag{2.120}$$

This equation is valid both for the loading bar position $x = D_{SL}$ and the mid-beam position $x = \frac{S}{2}$ since it contains the vertical displacement $w_{II}(x)$. Accordingly, this equation delivers two different calculated bending stiffnesses. The force F and the measured vertical displacement $w_{II}(x)$ have to be inserted as $\Delta\,F$ and $\Delta\,w_{II}(x)$ respectively. These values are taken from the force-displacement plot of each specimen tested. When presenting the results in Chapt. 4 and 5, the bending stiffness at mid-beam position using the measured displacement f_m is denoted as $B_{x,fm}$. The bending stiffness at loading bar position using f_s is further denoted as $B_{x,fs}$.

A third way to determine B_x is its calculation via measured strains in x-direction. The strain resulting from pure bending ε_b can be derived according to Nickel [3, pp. 42,43] using the upper side strain ε_u and the lower side strain ε_l:

$$\varepsilon_b = \frac{\varepsilon_l - \varepsilon_u}{2} \tag{3.1}$$

In further calculation, here also $\Delta\,\varepsilon_b$ is taken using $\Delta\,\varepsilon_u$ and $\Delta\,\varepsilon_l$ as gained from the force-strain plot. Equation (2.112) can be rewritten as:

$$B_x = -\frac{M}{w''} = \frac{M}{\kappa} \tag{3.2}$$

When considering pure bending the curvature κ is equal to the pure bending strain ε_b divided by the z-distance from the beam's mid-plane to one of its surface.

$$\kappa = \frac{\varepsilon_b}{\frac{t_{sw}}{2}} = \frac{2\,\varepsilon_b}{t_{sw}} \tag{3.3}$$

Inserting Eq. (3.3) into Eq. (3.2) and considering the bending moment being $\Delta M = \frac{\Delta F}{2} D_{SL}$ delivers the equation for calculating the bending stiffness $B_{x,\varepsilon}$ based on strain data.

$$B_{x,\varepsilon} = \frac{\frac{\Delta F}{2} D_{SL} t_{sw}}{2 \Delta \varepsilon_b} = \frac{\Delta F D_{SL} t_{sw}}{4 \Delta \varepsilon_b} \tag{3.4}$$

The second kind of stiffness to be determined is the transverse shear stiffness, represented by the shear modulus G_{xz}. As a shear force $Q = \frac{1}{2} F$ is acting in the beam area between the support and the loading bar (area I), there is also a shear force to be considered at the loading bar position $x = D_{SL}$. Hence, the measured vertical displacement f_s occurs as an interaction of a shear displacement $f_{s,sh}$ and a displacement resulting from pure bending $f_{s,b}$. The shear displacement can thus be determined as follows:

$$f_{s,sh} = f_s - f_{s,b} \tag{3.5}$$

The pure bending displacement $f_{s,b}$ is calculated via Eq. (2.119) using the bending stiffness as determined with the help of the strains $B_{x,\varepsilon}$. The strain based bending stiffness is used here due to two reasons. The first reason is that for the tests of five thick sandwich specimens the laser distance sensor has been removed from the test apparatus due to the danger of taking damage during specimen failure. So there are no data available for the usage of $B_{x,fm}$ for the respective specimens. The second reason is that $B_{x,fs}$ is considered to be less accurate as the resilience of the cross head and further parts of the test machine has significant influence on the measured machine path f_s. The shear strain $\gamma_{xz,sw}$ is further gained using the distance D_{SL}:

$$\gamma_{xz,sw} = \frac{\partial w_{sh}}{\partial x} = \frac{f_{s,sh}}{D_{SL}} \tag{3.6}$$

According to Wiedemann [22, pp. 223-227] the shear stiffness can be described by the quotient of the respective acting shear force $n_{sh,xz} = \frac{N_{sh,xz}}{b_{y,sw}}$ and shear strain. The shear force here is normalized by the sandwich's width $b_{y,sw}$. Since the shear modulus in general is defined as $G = \frac{\tau}{\gamma}$ with $\tau = \frac{N_{sh,xz}}{b_{y,sw} t_{sw}}$ the defined shear stiffness is divided by t_{sw} to obtain the shear modulus G_{xz} as a quantity of the unit $\frac{\mathrm{N}}{\mathrm{m}^2}$.

$$G_{xz} = \frac{n_{sh,xz}}{\gamma_{xz,sw}} \frac{1}{t_{sw}} = \frac{\frac{F}{2\,b}}{\gamma_{xz,sw}} \frac{1}{t_{sw}} \tag{3.7}$$

4 Experimental Results on Balsa Wood Material Behaviour

The results from the experiments described in the previous chapter contribute to the sandwich model calculation. So in this chapter the results are partly shown and the according implementation of the balsa wood behaviour into the analytical model is described.

By performing the experiments regarding the wood moisture, the influence of vacuum during the infusion process and of the resin infusion and curing on the geometry of balsa wood the main aim has been to get data that allow a correction of the total plate geometry within the model calculation. At this point it is necessary to mention that the model has two implemented ways to determine the final resulting geometry of the total infused plate. While the thickness of the infused plate is assumed to stay constant as it will be substantiated in this section, the in-plane dimensions (length and width) do change, so they have to be corrected. In the model these corrections affect the total plate size as it is measured after receiving and before infusion. With the mentioned corrections, the dimensions for the resulting infused plate are calculated. But the consideration of these plate corrections is no longer valid if the final resulting plate dimensions are defined by trimming the original plate, for example when specimens are cut out of the plate. The dimensions of a specimen are then seen as predefined in the model and no automatic plate correction is executed. Hence, a trimming mode can be set. The mode "Trimming to final Plate Geometry" enables to manually set the length and width of the final infused plate, e.g. of a specimen. Then the plate corrections are neglected. The other available mode is "Measures to be trimmed". Here the shortening in length and width by trimming can be defined. These Δ-values are subtracted from the plate dimensions in addition to the plate corrections, which are now active since the final dimensions are not predefined. By setting both Δ-values for length and width to zero, only the plate corrections are taken into account for the calculation of the final infused plate geometry.

4.0.1 Wood Moisture

The investigation of the behaviour of balsa wood concerning the moisture content showed an decrease both in length and width of the tested balsa samples with increasing moisture content. This measured correlation is in accordance with the expectation that balsa wood experiences a swelling as the cell walls expand with increasing moisture content. Less wood moisture in turn leads to a shrinkage of the balsa block.

The measured length, width and thickness of the samples are plotted against the moisture content. The measured wood moisture ranges from about 4 % to approximately 16 %. Then a linear regression line is applied to each series of data points. From each of the gained regression lines the gradient is determined. Afterwards all gradients are sorted by the density class that each sample is belonging to (see Table 3.1). For each density class the average dimension change gradients are determined. So there is one gradient k for each measured geometrical quantity per density class. Figure 4.1 illustrates the gained gradients k exemplarily for the medium-density class.

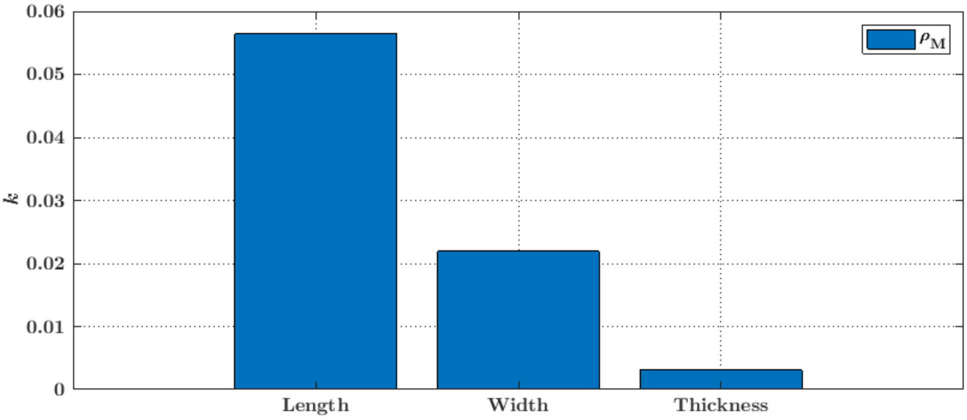

Figure 4.1: Dimension change gradient for medium-density balsa

The gradient k as shown for the medium-density balsa is representative for all three density classes as the gradient does not differ much. Due to the fact that the balsa samples used for the wood moisture experiment only cover a density range from 78.95 $\frac{\mathrm{kg}}{\mathrm{m}^3}$ to 179.32 $\frac{\mathrm{kg}}{\mathrm{m}^3}$ the average densities of samples of each density class are rather close to one another. Thus, it is reasonable that the swelling/shrinkage behaviour also does not differ that much. In addition it can be stated that in case of a reduction of the moisture content, the balsa wood's thickness is not affected significantly. Hence, the thickness is not changed in the model calculation.

The determined dimension change gradients are implemented into the model. For the calculation of the geometry change the model requires the input of the measured moisture content after receiving the core plate and shortly before infusion. Then the gradient k is used to perform a linear change of each the block's length and the block's width. Thus a Δ_{dim}-value for both dimensions is determined. With a given moisture content measured after receiving the plate H_1 and a moisture content measured before infusion H_2 the correction is done as follows:

$$\Delta_{dim} = k_{dim} \left(H_2 - H_1\right) \tag{4.1}$$

Previously in this thesis the assumption was stated that each single balsa block stays at its initial position, because it is fixed to the glass-fiber fabric at its bottom surface. Taking this assumption into account, the model determines the corrected total plate length by subtracting the change in length of one balsa block from the total measured plate length. This is equal to the shrinkage of half a block at each end in length. However, the correction is somewhat neglectable as the change in dimension does not exceed a change of about 0.2 mm at moisture contents of less than 10 % as usually have been measured without previous exposure to higher air humidity in the climate chamber.

4.0.2 Vacuum

The influence of balsa wood being exposed to vacuum before the actual resin infusion is simply related to the moisture content. By evacuating air from the balsa core plate's surface the core plate is expected to dry. This moisture reduction would then lead to a shrinkage of the plate. The performed experiment as described in Subsect. 3.1.2 provides the measured moisture content of each sample in dependence of time while being exposed to vacuum. The gained plots can be seen in Fig. 4.2.

It can be seen that all plotted curves tend to converge at a moisture content of about 10 %. While the loss of moisture during the first 30 min. seems to follow a larger gradient, the moisture content stays constant after another 30 min. of vacuum exposure. The model thus only calculates a geometry change per balsa block, if the initially

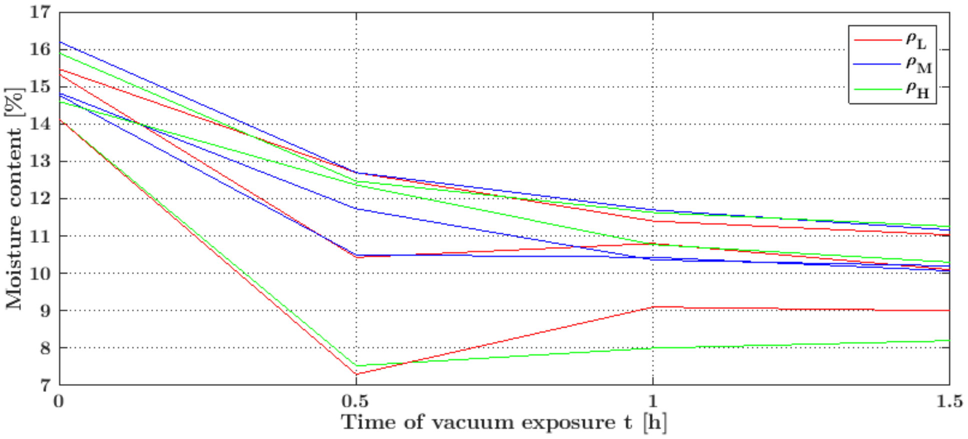

Figure 4.2: Moisture content in relation to vacuum exposure time

measured moisture content of the modelled plate is greater than 10 %. The correction is done in the same way as described in the previous section (see Eq. (4.1).

4.0.3 Resin Infusion and Curing

At this point the infused pure balsa plates shall be investigated in order to receive reasonable values for the resulting slit widths s_x and s_y and the plates' geometries. The validation of the model's mass calculation shall not be part of this subsection, since it is presented in the Chapt. 5.

The slit widths of the infused plate A has been measured by metallic rulers, which have been fixed at the lower side of the glass plate the infusion has been performed on. Both during the infusion process and after the curing detailed photographs have been made in order to investigate the slit width in axial and lateral direction. Figure 4.3 shows the the captured slits of plate A both before resin-infused and after infusion and curing.

The slit width that can be determined by the photographs does not exceed a width of roughly 0.5 mm. At first glance however, the resin-filled slits appear to be larger in width. The reason for that is the fact that the resin penetrates the outer edges of the balsa blocks and thus these edges are no longer distinguishable without closer look. The photograph of the dry balsa before infusion is used for specifying the setting for the zero opening slit width in the model as 0.2 mm.

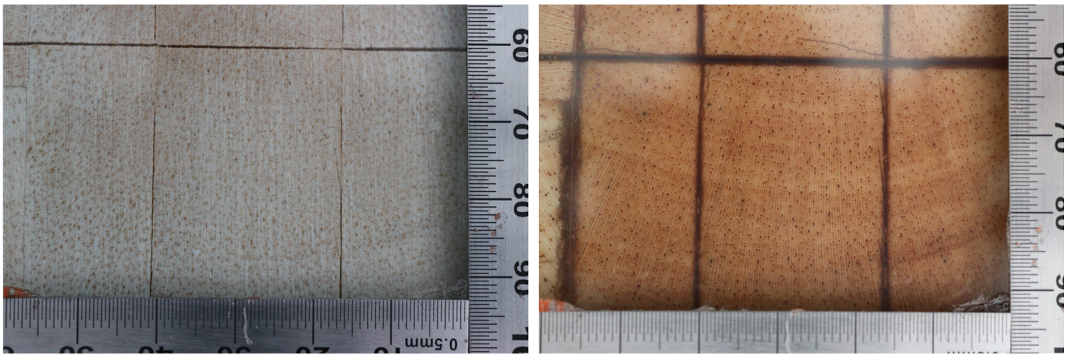

Figure 4.3: Photographs of plate A: (left) before infusion (right) after infusion and curing

It is obvious that this argumentation is not entirely satisfying. To closer investigate the actual slit width, plate C is spectated via an optical microscope. With the help of the respective software the longitudinal slit width s_x and the transverse slit width sy can then be measured directly on the micrograph. The measurements are done at five different positions across the plate's surface. The measured slit widths are listed in Table 4.1.

Table 4.1: Measured slit widths of plate C in longitudinal and transverse direction

	s_x [µm]	s_y [µm]
Pos. No.		
1	619.06	370.91
2	820.47	570.14
3	583.02	447.21
4	722.95	493.84
5	572.42	127.17

Practically seen there is no reason why the slit widths in longitudinal direction is different from the slit width in transversal direction, because the distribution of the different cell types in the plate's xy-plane can be seen as arbitrarily orientated and thus the shrinkage both in x-direction and y-direction is considered to be of equal amount. For an overall value as model input preference the arithmetic mean value is determined as $s_{mean} = 532.72\,\mu\text{m}$. The model input regarding the slit widths is an addition of the zero opening, the moisture correction and a defined widening due to resin and curing block shrinkage. As a resulting slit width of about 0.5 mm is preferred the zero opening and the resin influenced widening is set as 0.2 mm each. A moisture correction of about 0.1 mm is plausible.

5 Model Validation

The resulting masses and stiffnesses calculated by the model shall be compared to the experimental results. This also includes the mass calculation model validation, which is done by evaluating the resin-infused pure balsa core plates A, B and C. In addition one data example from the four point bending test is shown. For the purpose of comparison the model settings and its final calculation methods regarding the complete sandwich (not just the infused core) are presented in advance. The comparison itself is done in table form. Afterwards, the gained values and their reasons are discussed.

5.1 Comparison of Model Results and Experimental Results

At the beginning of this section the purely infused balsa plates denoted as A, B and C are modelled and the calculated masses are compared to the measurements m_{meas} in order to validate the different approaches that are implemented regarding mass calculation. The different approaches to be considered are the smearing approach and the geometrical approach. Additionally, it is distinguished between manual trimming and without trimming (i.e. w/o or with plate correction). As input parameter the density of the core is set as apparent nominal density ($148\,\frac{\mathrm{kg}}{\mathrm{m}^3}$ for BALTEK SB.100). The density of the cured resin is $1.131\,\frac{\mathrm{g}}{\mathrm{cm}^3}$. The zero slit width and the resin caused slit width is set as 0.2 mm following the argumentation from the previous chapter. On cell level the total fiber length L_f is defined as 650 µm, $h_{end,f}$ equals 70 µm. The ray cell length is 76 µm. The simple linear approach on penetration depth is used. Table 5.1 shows the comparison of the results.

The relative error is determined as error of the model with the measured mass as true value. The infusions of plates B and C have been documented strictly by measuring all contributing mass components throughout the infusion process. For plate A this has not been done. Since the data for plates B and C have been complete, those two

Table 5.1: Mass results from experiment vs. model results (infusion of pure balsa plates)

Plate	**A**	**B**	**C**
$\boldsymbol{m_{meas}}$ [g]	2869.6	986.56	547.61
Trimming manually			
$\boldsymbol{m_{Plate,sm}}$ [g]	2600.6	940.6	509.06
rel. Error [%]	-9.37	-4.66	-7.04
$\boldsymbol{m_{Plate,geom}}$ [g]	2639.5	962.8	509.8
rel. Error [%]	-8.02	-2.41	-6.9
w/o Trimming			
$\boldsymbol{m_{Plate,sm}}$ [g]	n.d.	944.7	505.1
rel. Error [%]	n.d.	-4.24	-7.76
$\boldsymbol{m_{Plate,geom}}$ [g]	n.d.	965.2	505.2
rel. Error [%]	n.d.	-2.16	-7.74

plates shall be in focus of this validation. Hence, there is no modelling done for plate A without trimming.

Besides the plate infusions the four point bending test with sandwich specimens is the main part of the model validation process as it considers the entire FRP sandwich. For each of the 16 specimens the vertical displacement is plotted against the force. This measurement is complemented by plotting the strain on upper and lower sandwich side at center position of each specimen. The manufactured specimens are numbered from Spec. 1 to Spec. 16. Spec. 1-8 are sandwiches with a nominal core thickness of 12.7 mm and Spec. 9-16 have a core of a doubled thickness of 25.4 mm. As an example, the plots from specimen no. 10 are shown (Fig. 5.1 and Fig. 5.2).

With regard to Fig. 5.2 it is important to mention that the used ΔF shall not include the non-linear part of the lower side strain plot. As previously described the bending stiffness B_x is determined in three different ways, taking into account the vertical displacement f_s, the vertical displacement f_m and the measured strains. The sandwich model however determines one value $B_{x,sw,model}$ by applying the classical laminate theory according to Eq. (2.106):

$$B_{x,sw,model} = E_{ij,sw}\, I_{sw} = b\,\frac{1}{D_{11}^{-1}} \tag{5.1}$$

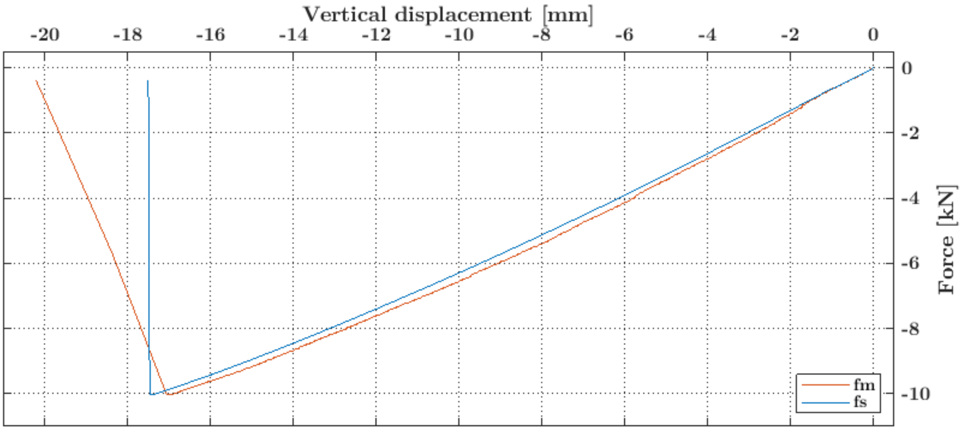

Figure 5.1: Force vs. vertical displacements (specimen no. 10)

In the calculation steps the resin-infused core is seen as one UD layer having the in-plane stiffnesses $E_{\parallel} = E_{x,sm}$ and $E_{\perp} = E_{y,sm}$. The smeared Young's moduli (index: sm) are the moduli as derived in Subsect. 2.4.2. The Poisson's ratio is determined by smearing the Poisson's ratio of wood as it is described in the literature of Gibson and Ashby [11, p. 420] and the Poisson's ratio of resin according to the volumes of the defined RVE for masses (Fig. 2.12). The UD layer thicknesses t_k are calculated with the help of a predefined fiber volume content (FVC) φ, the glass-fiber density ρ_f and the area per unit mass of the used glass-fiber layer $(\frac{m}{A})_f$.

$$t_k = \frac{(\frac{m}{A})_f}{\rho_f\,\varphi} \tag{5.2}$$

The fiber volume content is defined as the volume fraction of the fibers' volume respective to the total volume of the FRP composite [16, p. 162]. When subtracting the fibers' volume from the total FRP composite, the matrix volume remains. Within the model the FVC is a parameter that has to be predefined manually. The quantity of fibers in relation to the matrix quantity can also be defined by the respective masses. According to Schürmann the fiber mass content (FMC) ψ is defined as follows [16, p. 167]:

$$\psi = \frac{\rho_f\,\varphi}{\rho_f\,\varphi + \rho_R\,(1-\varphi)} \tag{5.3}$$

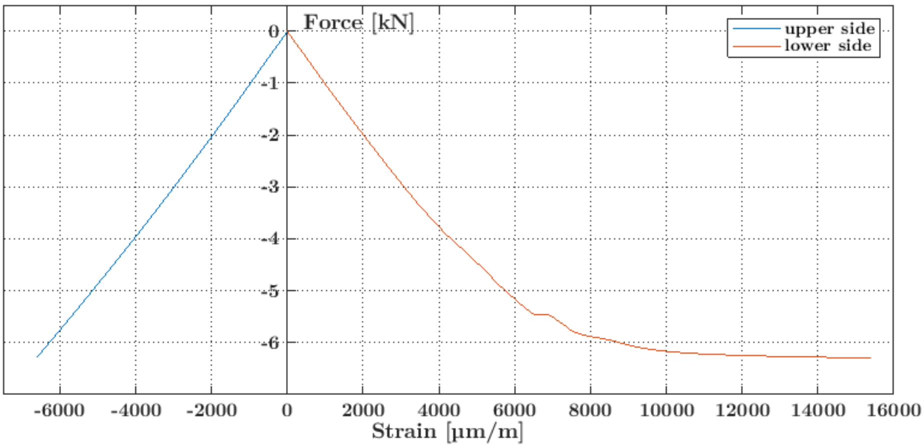

Figure 5.2: Force vs. strains (specimen no. 10)

The FMC is used within the model for the determination of the face sheet mass of the sandwich. With the total mass of glass-fiber per face sheet $m_{f,fs}$ the total mass of the single face sheet m_{fs} is obtained.

$$m_{fs} = \frac{m_{f,fs}}{\psi} \tag{5.4}$$

Returning to the model's sandwich stiffness calculation again there is the need to determine the shear modulus $G_{xz,sw,model}$. Here a relation given by Allen [23, p. 137] is used. For orthotropic faces and core and faces of equal thickness and similar material the shearing stiffness D_{Qx} can be determined as:

$$D_{Qx} = G_{C,xz,sm} \frac{d^2}{t_C} \tag{5.5}$$

Here, d is denoted as the distance between the face sheets' mid-planes and $G_{C,xz,sm}$ is the smeared shear modulus of the resin-infused balsa wood core (see Eq. (2.63). By dividing D_{Qx} by the sandwich thickness t_{sw} the model's shear modulus for the sandwich is gained.

$$G_{xz,sw,model} = D_{Qx} \frac{1}{t_{sw}} \tag{5.6}$$

Now all necessary quantities for both the experimental results of the sandwich and the model results of the sandwich are derived. The model calculation is done with the manual trimming mode. Hence, no plate corrections are done. Further the model requires the predefinition of the fiber volume content φ. The specimens' upper and lower face sheet thicknesses have been measured before performing the four point bending test. With this data, the FVC could be determined with an IWES internal calculating tool. The measured fiber volume contents then are averaged and the standard deviation is subtracted and added to the mean value. By doing this a minimum FVC φ_{min} and a maximum FVC φ_{max} are determined for each the thin sandwich plates and the thick sandwich plates. For the model results that means that two values for each quantity (mass m, bending stiffness B_x and transverse shear stiffness G_{xz}) are taken as the value range in which the model's results are located. For the thin sandwich specimens (Spec. No. 1-8) φ_{min} and φ_{max} are determined as 0.4802 and 0.53. For the thick sandwich specimens (Spec. No. 9-16) φ_{min} and φ_{max} are determined as 0.49089 and 0.52.

Furthermore, the measured machine path, which is assumed to represent the vertical displacement at loading bar position is finally corrected with the help of test data in a way that the resilience of the test machine's cross-head is taken into account. The measured machine path f_s thus is corrected towards smaller values.

Table 5.2 shows the results for the masses, Table 5.3 those for the bending stiffnesses and Table 5.4 those for the transverse shear stiffnesses.

Table 5.2: Masses: experiment vs. model

	Exp.	**Model**			
	$\boldsymbol{m}$ [g]	$\boldsymbol{m_{sm,min}}$ [g]	$\boldsymbol{m_{sm,max}}$ [g]	$\boldsymbol{m_{geom,min}}$ [g]	$\boldsymbol{m_{geom,max}}$ [g]
Spec. No.					
1	505.03	492.35	514.23	492	513.88
2	506.46	492.01	513.88	491.71	513.58
3	502.02	484.14	505.66	484.93	506.45
4	526.29	502.78	525.13	503.33	525.68
5	480.69	484.27	505.8	485.05	506.57
6	509.71	489.97	511.75	489.96	511.73
7	511.18	490.94	512.76	490.79	512.61
8	498.98	492.05	513.92	491.75	513.62
9	636.19	635.13	648.23	641.57	654.67
10	608.28	599.32	611.68	604.15	616.51
11	646.88	609.58	622.15	616.6	629.17
12	590.87	619.08	631.85	624.38	637.15
13	621.94	611.27	623.88	617.99	630.6
14	621.44	611.49	624.1	618.17	630.78
15	637.12	643.74	657.02	648.63	661.9
16	557.82	593.03	605.26	599.01	611.23

Table 5.3: Bending stiffnesses: experiment vs. model

	Exp.			**Model**	
	$\boldsymbol{B_{x,fm}}$ [N m^2]	$\boldsymbol{B_{x,fs}}$ [N m^2]	$\boldsymbol{B_{x,\varepsilon}}$ [N m^2]	$\boldsymbol{B_{x,min}}$ [N m^2]	$\boldsymbol{B_{x,max}}$ [N m^2]
Spec. No.					
1	393.94	373.53	411.14	426.25	439.67
2	368.81	368.37	408.73	425.96	439.37
3	348.84	378.22	410.81	419.4	432.6
4	385.34	373.97	323.24	435.54	449.25
5	380.73	364.21	401	419.5	432.71
6	394.91	381.56	410.74	424.44	437.81
7	386.68	373.5	392.94	425.03	438.41
8	384	380.09	430.95	426.25	439.67
9	1224.04	1143.29	1341.08	1533.87	1544.21
10	1145.67	1088.46	1224.43	1445.63	1455.37
11	1240.44	1147.04	1427.31	1471.24	1481.16
12	n.d.	1094.22	1415.04	1492.39	1502.45
13	n.d.	1124.93	1417.37	1477.14	1487.1
14	n.d.	1134.6	1382.43	1478.56	1488.53
15	n.d.	1136.35	1467.38	1552.78	1563.25
16	n.d.	1047.44	1373.85	1432.21	1441.86

Table 5.4: Transverse shear stiffnesses: experiment vs. model

	Exp.	**Model**	
	$\boldsymbol{G_{xz}}$ $\left[\frac{\mathrm{N}}{\mathrm{mm}^2}\right]$	$\boldsymbol{G_{xz,min}}$ $\left[\frac{\mathrm{N}}{\mathrm{mm}^2}\right]$	$\boldsymbol{G_{xz,max}}$ $\left[\frac{\mathrm{N}}{\mathrm{mm}^2}\right]$
Spec. No.			
1	180.69	316.99	318.46
2	165.63	316.99	318.46
3	213.88	316.99	318.46
4	-103.35	316.99	318.46
5	179.12	316.99	318.46
6	238.24	316.99	318.46
7	335.79	316.99	318.46
8	141.72	316.99	318.46
9	191.56	308.77	309.02
10	256.69	308.77	309.02
11	149.78	308.77	309.02
12	122.02	308.77	309.02
13	139.67	308.77	309.02
14	162.74	308.77	309.02
15	123.37	308.77	309.02
16	116.7	308.77	309.02

5.2 Discussion

Regarding the masses the model values generally are in good agreement with the actual measured masses. The infused pure balsa plates A, B and C (Table 5.1) all show a relative error of less than 10 %. When comparing the relative errors with regard to the two different used calculation approaches, the geometrical approach consistently leads to lower errors independent of the plate's thickness. Additionally, it can be seen that the model's mass is lower than the measured mass at all three plates. That indicates that the mass estimation for the pure resin-infused balsa core plate leads to lighter result than it is in reality. With respect to proper mass estimation during the design phase of a rotor blade, this is actually worse than estimating a higher mass because the need of accurate models on mass estimation rather originates from mass underestimation since it is attended by higher actual acting mass loads. However, the low number of tested plates here is not representative, but gives an impression, if the used approaches tend to deliver proper mass results. The geometrical approach here leads to higher masses than the smearing approach for the thick plate B, but both approaches are somewhat equal, when comparing the modelled masses of the thin plate C.

The model calculation of the total mass of sandwich plates includes the face sheet mass. So by weighing the manufactured sandwich specimens it is no longer distinguishable, what the actual mass of the infused core is. Hence, the comparison of the sandwich masses (Table 5.2) can only contribute to the validation of the total mass determination. The comparison of the two applied approaches considering the core thickness shows a tendency of the smearing approach to deliver lower results with increasing core thickness. This fact however does not lead to a more critical underestimation for the sandwich in consequence since some of the thick specimen even have a mass below the model's minimum mass. So with increasing core thickness the smearing approach seems to be more accurate.

Regarding the bending stiffness (Table 5.3) the values, which have been determined by applying the bending line theory are not in good agreement with the range given by the model, whereas the bending stiffness $B_{x,\varepsilon}$ comes close to the model's data. This is plausible because by measuring the vertical deflection as the test machine path, the resilience of the cross head may lead to a higher measured vertical deflection. The strain gauges are independent of any resilience that may falsify the measured displacement. So in comparison with the strain based bending stiffness the model is quite accurate, although delivering slightly higher stiffnesses.

The shear stiffness represented by the transverse shear modulus shows the largest discrepancy between experimental and model results (Table 5.4). The obtained difference might be explained by two reasons. On the one hand the experimental shear stiffness is assumed to be determined as too low. Since its calculation bases on the measured test machine path f_s it can be shown that a correction of less than 1 mm already has a significant influence on the transverse shear stiffness towards higher stiffnesses that come close to the model's results. Hence, the cross head resilience is critical here. On the other hand the model's shear modulus almost entirely equals the smeared transverse shear modulus $G_{C,xz,sm}$ of the infused core. The face sheets' contribution to the transverse shear stiffness is neglectable as they carry mainly tensile loads. The smeared shear stiffness in turn depends on the respective shear modulus of balsa wood $G_{C,xz}$. This quantity has been taken from the literature of Gibson and Ashby and is based on a semi-empirical equation for wood in general [11, p. 418]. The actual shear modulus of balsa wood might be lower, so the agreement of experiment and model could be achieved by corrections in both experimental and model-based calculation. Since the shear modulus is a material constant, the low difference of the model's shear modulus regarding the plate thickness can be seen as the shear carrying amount of the face sheets.

6 Conclusion and Future Research

The analytical model for the resin-infused balsa wood core as developed within the scope of this thesis is supposed to deal with the two aims of modelling accurately the resulting mass and the stiffnesses of a FRP sandwich plate. Experiments show that the mass estimation by the model is quite accurate both when sandwich plates and pure resin-infused balsa cores are modelled. The derived pure geometrical approach does not show a significant difference in comparison to the smearing approach.

The smeared stiffnesses are highly depending on the stiffnesses of pure balsa. Thus the model's accuracy for the transverse shear modulus calculation is less accurate, giving values roughly increased by a factor of 2 in relation to the experimental results. Furthermore, when performing bending tests the application of strain gauges is preferable.

For future research it remains to explicit validate the smeared stiffness of the infused balsa core plate. This validation could not be done by testing the sandwich specimens, due to the fact that experimental results gained from the four point bending tests describe the whole sandwich inclusive the face sheets. Hence further experiments are necessary to determine the in-plane and out-of-plane stiffnesses of resin-infused balsa wood plates. These tests shall include both tensile tests and shear tests. In addition, the tensile and shear stiffnesses of pure balsa wood shall be investigated experimentally, in particular the dependency on the wood's orientation. Another aspect of future extension of the model is the implementation of plate curvature. The curved plate is assumed to take up a significantly higher amount of resin due to the widening of the slits. When regarding the experimental set-up for four point bending tests it could be shown that the test machine's resilience and the resilience of the test apparatus influence the machine path as measured by the LVDT. For more reliable bending tests a possibility has to be found to measure the vertical displacement at the contact position of specimen and loading bar.

Bibliography

[1] Bundesverband WindEnergie e.V. (BWE): *Zahlen und Fakten, Grafiken: Factsheet: Windenergie in Deutschland 2019, Stromerzeugung aus Windenergie, Anteil an der Stromproduktion.* **https://www.wind-energie.de/themen/zahlen-und-fakten/** Last Access: September 5, 2020 (2019)

[2] Verein Deutscher Ingenieure (VDI), VDI Blog: *Daher weht der Wind! - 5 Fragen über Windkraftanlagen (Interview, Liersch J.).* **https://blog.vdi.de/2018/11/daher-weht-der-wind/** Last Access: September 6, 2020 (2018)

[3] Nickel, A.: *Optimierung der Designparameter von GFK-Kern-Verbunden unter Berücksichtigung der Harzaufnahme des Kerns.* Diplomarbeit, Technische Universität Berlin (2011)

[4] Fraunhofer Institute for Wind Energy Systems IWES (internal): *Website Fraunhofer IWES.* **https://www.iwes.fraunhofer.de/en.html** Last Access: September 8, 2020 (2020)

[5] Fraunhofer-Gesellschaft (internal): *Zahlen und Fakten - Auftragsforschung für Wirtschaft und Staat.* **https://www.fraunhofer.de/de/ueber-fraunhofer/profil-struktur/zahlen-und-fakten.html** Last Access: September 8, 2020 (2020)

[6] Antoniou, A.: *PowerPoint-Präsentation: Rotor von Windenergieanlagen - Aerodynamik, Strukturen und Fertigung, Materials-I: Einführung in Rotorblattmaterialien.* IWES internal

[7] Rosemeier, M., Buriticá, P., Antoniou, A.: *Impact of resin uptake of core materials on buckling of wind turbine blades.* Journal of Physics: Conference Series 1037, 042001 (2018)

[8] Tan, H., Pillai, K. M.: *Blast Protection of Civil Infrastructures and Vehicles Using Composites.* Woodhead Publishing, **https://www.sciencedirect.com/topics/engineering/liquid-composite-moulding** Last Access: September 8, 2020 (2010)

[9] Vural, M., Ravichandran, G.: *Microstructural aspects and modeling of failure in naturally occurring porous composites.* Mechanics of Materials 35, 523–536 (2003)

[10] Da Silva, A., Kyriakides, S.: *Compressive response and failure of balsa wood.* International Journal of Solids and Structures 44, 8685–8717 (2007)

[11] Gibson, L. J., Ashby, M. F.: *Cellular Solids: Structure and Properties.* (2nd ed., Cambridge Solid State Science Series), Cambridge University Press, Cambridge (1997)

[12] Easterling, K. E., Harrysson, R., Gibson, L. J., Ashby, M. F.: *On the mechanics of balsa and other woods.* Proceedings of the Royal Society London A 383, 31–41 (1982)

[13] Borrega, M., Ahvenainen, P., Serimaa, R., Gibson, L.: *Composition and structure of balsa (Ochroma pyramidale) wood.* Wood Science and Technology 49, 403-420 (2015)

[14] Shishkina, O., Lomov, S. V., Verpoest, I., Gorbatikh, L.: *Structure–property relations for balsa wood as a function of density: modelling approach.* Archive of Applied Mechanics 84, 789–805 (2014)

[15] Alcan Composites (now 3A Composites): *PowerPoint-Präsentation: Einführung in Airex und Baltek Kernmaterialien.* Accessed by: Gaugler & Lutz oHG (2003)

[16] Schürmann, H.: *Konstruieren mit Faser-Kunststoff-Verbunden.* Springer-Verlag Berlin Heidelberg (2005)

[17] Deutsches Institut für Normung e.V. (DIN): *DIN 53 293 Prüfung von Kernverbunden, Biegeversuch.* (1982)

[18] American Society for Testing and Materials International (ASTM International): *ASTM C393/C393M-16 Standard Test Method for Core Shear Properties of Sandwich Constructions by Beam Flexure.* (2016)

[19] ingenieurkurse.de - examio GmbH: *Baustatik 1: Differentialgleichung der Biegelinie.* **https://www.ingenieurkurse.de/baustatik-1/verformungen/verformung-infolge-biegung/differentialgleichung-der-biegelinie.html** Last Access: September 10, 2020

[20] Simone (Author of www.befestigungsfuchs.de): *Das Schwinden und Quellen von Holz.* **https://www.befestigungsfuchs.de/blog/das-schwinden-und-quellen-von-holz/** Last Access: September 6, 2020 (2017)

[21] Nawab, Y., Shahid, S., Boyard, N., Jacquemin, F.: *Chemical shrinkage characterization techniques for thermoset resins and associated composites.* Journal of Materials Science 48, 5387–5409 (2013)

[22] Wiedemann, J.: *Leichtbau - Elemente und Konstruktion.* Springer-Verlag (2007)

[23] Allen, H. G.: *Analysis and Design of Structural Sandwich Panels.* Pergamon (1969)

Appendix

Appendix A

Technical Data Sheet

SAERTEX
E-Glass X-E-778g/m^2-1270mm

TECHNISCHES DATENBLATT ENTWURF

Art.-Nr.	**20006456**	**Art.-Bezeichnung**	**X-E-778g/m²-1270mm**
Textile Struktur 7006068		**SAERTEX®**	

ARTIKELAUFBAU (nach EN 13473-1)

Lage	Konstruktion	Flächengewicht	Toleranz	Material
4	45 °	384 g/m²	+/- 5,0 %	E-Glas 600 tex
3	90 °	3 g/m²	+/- 5,0 %	E-Glas 68 tex
2	0 °	1 g/m²	+/- 5,0 %	E-Glas 34 tex
1	-45 °	384 g/m²	+/- 5,0 %	E-Glas 600 tex
Nähfaden		6 g/m²	+/- 1 g/m²	PES [Polyester] 76 dtex

Faserinput kann individuell festgelegt werden

WEITERE EIGENSCHAFTEN

Nähfeinheit	5,0	Nähbindung	Franse	Breite (nominal)	1.270 mm
Stichlänge	2,60 mm	Gesamttoleranz	5,1 %	Gesamtflächen-Gewicht	778 g/m²

Kennfaden[1] 7 ST gelb

[1]Position kann individuell festgelegt werden

Etikettierung	Jede Rolle ist mit einem Etikett in der Hülse versehen. Ein weiteres Etikett befindet sich außen auf der Folie oder dem Karton.
Verpackung (Standard)	Jede Rolle ist in Folie verpackt und auf eine Papphülse gewickelt. Weitere Verpackungsoptionen können individuell festgelegt werden.
Lagerempfehlung	Bei Orginalverpackung: Temperatur 15-35°C und 20-80% Luftfeuchtigkeit. Keine Feuchtigkeit und direktes Sonnenlicht. Um Probleme mit Luftfeuchtigkeit oder elektrostatischer Ladung zu vermeiden, sind Gelege unabhängig von den Lagerbedingungen mind. 24h vor der Verarbeitung zu konditionieren.

Appendix B

Technical Data Sheet

HEXION
Epikote^{TM} Resin MGS RIMR 035C and Epikure Curing Agent MGS RIMR036, 0366, 037, 038, 038F

Technical Data Sheet

Epikote™ Resin MGS RIMR 035C and Epikure Curing Agent MGS RIMR036, 0366, 037, 038, 038F

Application

EPIKOTETM Resin MGSTM RIMR035c is a low-viscous infusion resin system approved by German Lloyd and can be used for processing of glass, carbon and aramide fibres. Due to its excellent mechanical properties, this system is suitable for the production of components featuring high static and dynamic loadability.

The range of pot lives is between approx. 2 hours and approx. 5.5 hours. Curing at higher temperatures (up to approx. 80-100°C) is possible, depending on laminate thickness and geometry of the parts to be manufactured.

The infusion resin system does not contain any unreactive components. The raw materials used feature a very low vapour pressure. This permits processing of the material under vacuum even at elevated temperatures. For processing at elevated temperatures lower reactive curing agents like RIMH037 and especially RIMH038 are available in order to keep exotherm temperatures during curing at a low level.

The optimum processing temperature is in the range of 20°C to 35°C. Higher temperatures are possible, but will shorten pot life. A temperature increase of 10°C will approx. halve the pot life. Different temperatures during processing are not known to have significant impact on the mechanical properties of the cured product.

All curing agents except of RIMH038F (F = free of pigment) are coloured for easier identification of a correct mixing process. Although unlikely, deviations in colour are possible (e.g. due to UV radiation after longer exposure to sun light), but are not known to have an effect on the processing and final properties of the material.

Compatibility problems are not to be expected in combination with UP gelcoats, coatings (e.g. PUR-based), etc. However, comprehensive tests are indispensable.

Although RIMR035c is very unlikely to crystallize at low temperatures, storage conditions of 15°C - 30°C and low humidity are recommended. If crystallisation of either component should be observed, it can be removed by warming up while stirring.

Slow warming up to approx. 50 – 60°C in an oven or heating cabinet and stirring or shaking will clarify the contents of the container without any loss of quality. Use only completely transparent products. Before warming up, open containers slightly to permit equalization of pressure. Caution during warm-up! Do not warm up over an open flame! While stirring up use safety equipment (gloves, eyeglasses, respirator equipment, long sleeves and trousers, safety shoes).

After dispensing material, the containers must again be closed carefully, to avoid contamination or absorption of water. All amine hardeners show a chemical reaction when exposed to air, known as „blushing“. This reaction is visible as white carbamide crystals, which could make the materials unusable.

The materials have a shelf life of minimum 2 years, when stored in their originally sealed containers.

The relevant industrial safety regulations for the handling of epoxy resins and curing agents and our instructions for safe processing are to be observed.

Specifications

		Infusion resin RIMR035c
Density 1)	$[g/cm^3]$	1.11 – 1.14

Density	[g/cm^3]	[illegible]
Viscosity 1)	[mPa·s]	1000 – 1500
Refractory index 1)	[–]	1,5530 – 1,5580

		Curing agent		
		RIMH036	RIMH0366	RIMH037
Density 1)	[g/cm^3]	0,93 – 0,96	0,92 – 0,96	0,92 – 0,96
Viscosity 1)	[mPa·s]	5 – 25	5 – 25	5 – 25
Refractory index 1)	[–]	1,460 – 1,465	1,458 – 1,467	1,458 – 1,464
Pot life 2)	[min]	110 – 170	150 – 250	190 – 290
$T_{G,\,mid,\,pot}$	[°C]	Approx. 80 – 85 (unconditioned)		

		Curing agent
		RIMH038 / RIMH038F
Density 1)	[g/cm^3]	0,91 – 0,95
Viscosity 1)	[mPa·s]	5 – 25
Refractory index 1)	[–]	1,460 – 1,463
Pot life 2)	[min]	240 – 330
$T_{G,\,mid,\,pot}$	[°C]	Approx. 80 (unconditioned)

Measuring conditions:

1) measured at 25°C

2) measured in 30°C water bath, 100g sample

Characteristics

Approval	DNV-GL SE (Germanischer Lloyd)
Application	Rotor blades for wind energy turbines, boat and shipbuilding, sports and recreation equipment, model construction, tooling
Operational temperature	-60°C to +70°C after heat treatment
Processing	Generally infusion at temperatures between 15°C and 50°C, depending on production parameters
Features	Low viscosity, extremely long pot life, excellent cost performance ratio
Storage	Shelf life of 24 months in originally sealed containers

Temperature

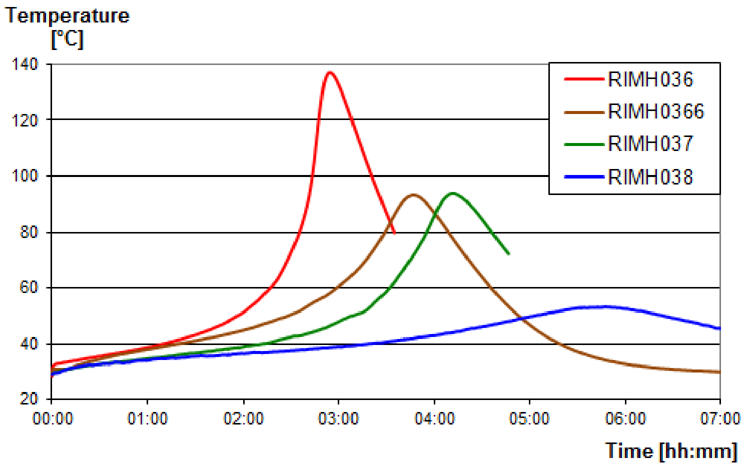

Measuring conditions: 100g mixture at 30°C in a water basin

Water (e.g. high humidity or contained in the fabrics) can cause an acceleration of the resin/curing agent reaction and influence mechanical properties.
Do not mix large quantities – particularly of higher reactive systems – at elevated processing temperatures. As the heat dissipation in the mixing container is very slow, the contents will be heated up by the reaction heat (exothermic resin-curing agent reaction) rapidly. This can result in temperatures of more than 200°C in the mixing container, which may cause smoke-intensive burning of the resin mass.

TG DEVELOPMENT

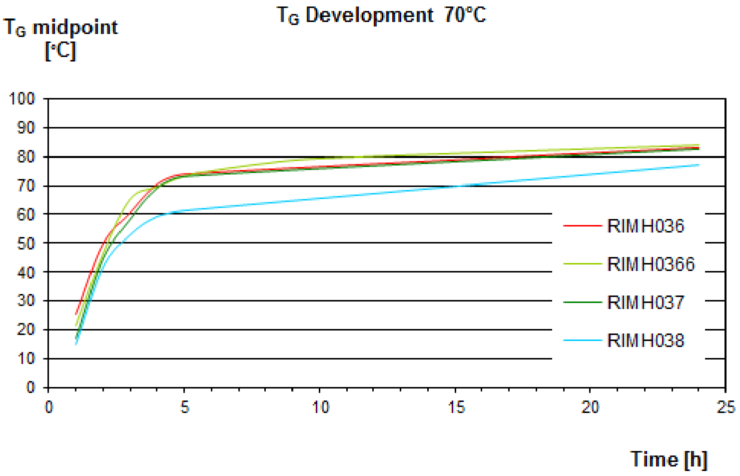

Measuring conditions: DSC, $T_{G,\ \mathrm{midpoint}}$ at 70°C cure according to MMS 4000

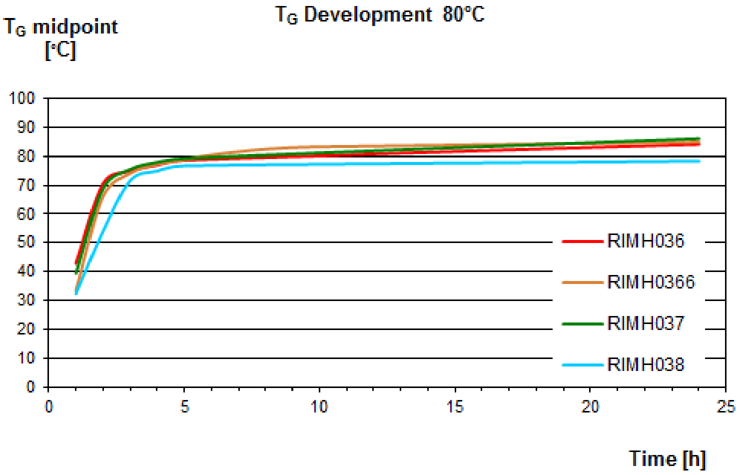

Measuring conditions: DSC, $T_{G,\ \mathrm{midpoint}}$ at 80°C cure according to MMS 4000

Mechanical Data

Mechanical data		
Density DIN EN ISO 1183-1	[g/cm^3]	Approx. 1,15
Flexural strength DIN EN ISO 178	[MPa]	Approx. 115
Modulus of elasticity DIN EN ISO 178	[GPa]	Approx. 3,1
Tensile strength DIN EN ISO 527-2	[MPa]	Approx. 70
Elongation at break DIN EN ISO 527-2	[%]	7 - 10
Water absorption at 23°C DIN EN ISO 175	24h [%] 7d [%]	Approx. 0,20 Approx. 0,40
Curing: 8h 70°C		

Advice:

Mechanical data are typical for the combination of infusion resin RIMR035C with curing agent RIMH037. Data can differ in other applications.

MIXING RATIOS

	RIMR035c with all curing agents
Parts by weight	100 : 28 ± 2
Parts by volume	100 : 34 ± 2

The mixing ratio stated must be observed carefully. Adding more or less curing agent will not result in a faster or slower cure, only incomplete curing with limited performance, that can not be corrected in any way.

Resin and curing agent must be mixed carefully. Mix until no clouding is visible in the mixing container. Special attention must be paid to the walls and bottom of the mixing container.

VISCOSITY DEVELOPMENT

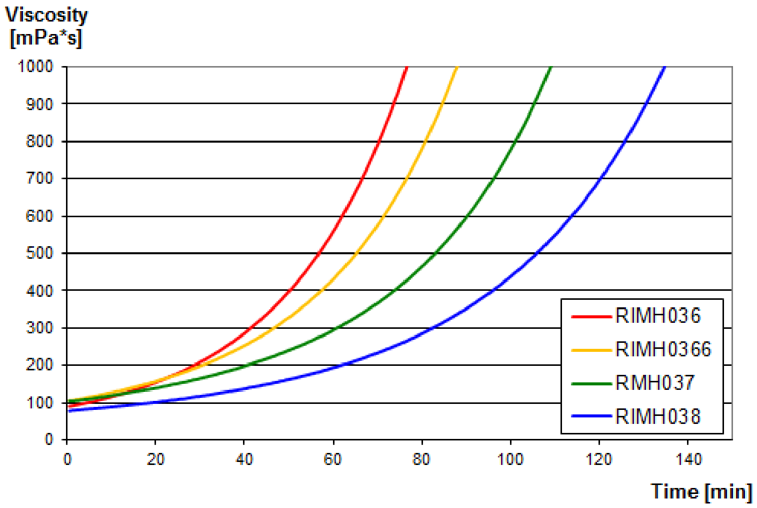

Measuring conditions: 40°C, cone-plate configuration, gap d=0,1 mm

VISCOSITY OF MIXTURE

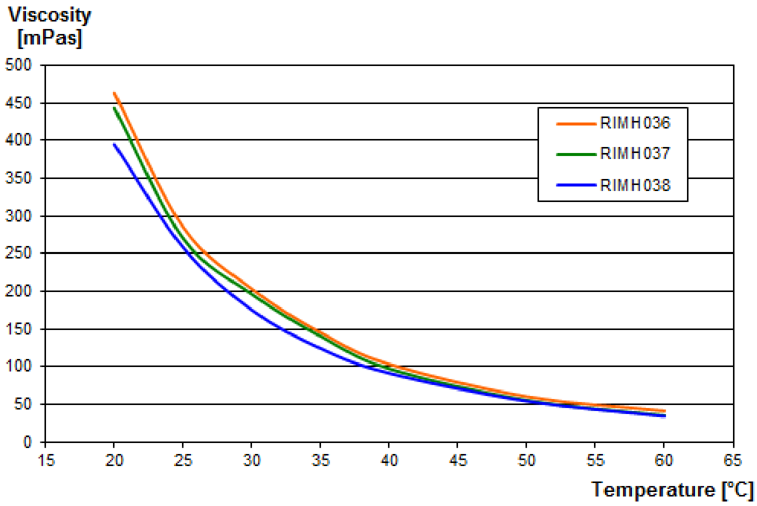

Measuring conditions: 100g mixture at 30°C in a water basin